Static response of coated microbubbles compressed between rigid plates: Simulations and asymptotic analysis including elastic and adhesive forces

A. Lytra, and N. Pelekasis

Citation: Physics of Fluids **30**, 030711 (2018); doi: 10.1063/1.5011175
View online: https://doi.org/10.1063/1.5011175
View Table of Contents: http://aip.scitation.org/toc/phf/30/3
Published by the American Institute of Physics

PHYSICS OF FLUIDS **30**, 030711 (2018)

Static response of coated microbubbles compressed between rigid plates: Simulations and asymptotic analysis including elastic and adhesive forces

A. Lytra and N. Pelekasis[a)]
Department of Mechanical Engineering, University of Thessaly, Volos 38334, Greece

(Received 30 October 2017; accepted 26 February 2018; published online 19 March 2018)

The static response of coated microbubbles is investigated with a novel approach employed for modeling contact between a microbubble and the cantilever of an atomic force microscope. Elastic tensions and moments are described via appropriate constitutive laws. The encapsulated gas is assumed to undergo isothermal variations. Due to the hydrophilic nature of the cantilever, an ultrathin aqueous film is formed, which transfers the force onto the shell. An interaction potential describes the local pressure applied on the shell. The problem is solved in axisymmetric form with the finite element method. The response is governed by the dimensionless bending, $\hat{k}_b = k_b/\left(\chi R_0^2\right)$, pressure, $\hat{P}_A = (P_A R_0)/\chi$, and interaction potential, $\hat{W} = w_0/\chi$. Hard polymeric shells have negligible resistance to gas compression, while for the softer lipid shells gas compressibility is comparable with shell elasticity. As the external force increases, numerical simulations reveal that the force versus deformation (f vs d) curve of polymeric shells exhibits a transition from the linear O(d) (Reissner) regime, marked by flattened shapes around the contact region, to a non-linear $O(d^{1/2})$ (Pogorelov) regime dominated by shapes exhibiting crater formation due to buckling. When lipid shells are tested, buckling is bypassed as the external force increases and flattened shapes prevail in an initially linear f vs d curve. Transition to a curved upwards regime is observed as the force increases, where gas compression and area dilatation form the dominant balance providing a nonlinear regime with an $O(d^3)$ dependence. Asymptotic analysis recovers the above patterns and facilitates estimation of the shell mechanical properties. *Published by AIP Publishing.* https://doi.org/10.1063/1.5011175

I. INTRODUCTION

Coated microbubbles (MBs), also known as contrast agents, have emerged as powerful contrast enhancers in medical imaging via ultrasound[1,2] and as drug delivery vectors[3,4] with highly localized impact on selected tissue. Their viscoelastic coating plays a central role in stabilizing them against dissolution, while adding targeting ligands along with an extra oil layer dissolving the therapeutic agent allows for efficient targeting and drug release[3–5] near specific tissue where therapeutic treatment is required. Coated MBs have an initial diameter from 1 to 10 μm, and the shell coating is an elastic biomaterial with thickness 5-50 nm. The core contains a gas phase, usually nitrogen, CO_2, or perfluorochemicals[6] which produces the local density gradient that is vital for the ultrasound. Two major families of coated microbubbles are normally employed, namely, those coated by polymeric and lipid shells. The former type shells are characterized by larger area dilatation modulus; hence, they are identified as "hard," whereas the latter are characterized by, relatively, smaller area dilatation; hence, they are identified as "soft" and more deformable shells. It is not only their small size that makes microbubbles suitable for the visualization of very small blood capillaries but also their ability to oscillate nonlinearly in response to ultrasound waves near the walls of small capillaries that mostly behave as linear scatterers.[7–9] As a result, both numerical[9] and experimental studies[6,10] suggest that a strong backscatter signal is generated during an ultrasound measurement that is strongly dependent on the shell properties (elasticity, thickness, material non-linearity, viscosity, etc.). Therefore, accurate estimation of their elastic properties, namely, Young's modulus (E) and bending modulus (k_b), is a key to design and optimize their response in the vascular bed.[11,12] This is typically made possible via accurate estimation of their resonance frequencies pertaining to volume pulsation,[8–11] particularly so for freely circulating MBs. In a similar fashion, the modulation of the resonance frequency of trapped microbubbles, due to their adhesion on pathogenic tissue, allows for identification of the latter during *in vivo* measurements as well as optimized visualization and localized delivery of the drug payload.[3,13]

Estimation of the viscoelastic properties of lipid shells, in particular, via acoustic measurements suffers from inherent complications[14,15] due to the strain softening nature of the shell.[9,16,17] More specifically, lipid monolayer shells tend to become softer during expansion due to the reduction in their surface density.[16,18,19] This tendency is reflected in the preferential excursion from equilibrium that is often observed in the expansion phase of their pulsation[16,18] in response to an acoustic disturbance. However, lipid shells also exhibit the opposite tendency when subjected to an acoustic disturbance, namely, they tend to pulsate mainly at compression,

a)Author to whom correspondence should be addressed: pel@uth.gr

"compression only behavior,"[14,15] that is typically associated with shells that become softer during compression.[9] The latter behavior is also associated with deformation and shell buckling;[14,15] hence, its accurate description involves a large number of shell properties which explains the lack of reproducibility in estimates of shell elasticity based on acoustic measurements.

Static measurements on the other hand involve a smaller number of parameters that are easier to control. To this end, atomic force microscopy (afm) experiments have been proven to be a reliable and successful tool for the characterization of the elastic properties for both types of coatings, in the form of force-deformation curves (to be referred to as f-d henceforth for brevity). In particular, Lulevich *et al.*[20] measured Young's modulus of hollow polyelectrolyte multilayered microcapsules of relatively small shell thickness using (afm). The capsules were seen to behave like elastomers with E on the order of 1-100 MPa and exhibited a nonlinear response, $f \sim d^3$, especially at relatively large deformations. The latter value was estimated by fitting the experimental f-d curve, obtained mainly at large deformations, against a model that takes shell stretching in the bulk of the shell and away from the contact region as the dominant recipient of the external force. This approach was similar to the one adopted by Shanahan[21] in an earlier study aiming at obtaining estimates of the adhesion energy of elastic membranes. In an ensuing study, Elsner *et al.*[22] studied similar shells, albeit with smaller relative thickness with respect to the shell radius, and found a predominantly linear response, $f \sim d$, for deformations on the order of shell thickness, also known as Reissner[23] regime, followed by a nonlinear response curve, $f \sim d^{1/2}$, corresponding to buckled shells in the region where the force from the cantilever is applied, as first pointed out by Pogorelov.[24] Simulations using the Abaqus software package verified this pattern. As will also be seen in the present study, the latter two regimes signify response patterns with stretching and bending resistance balancing each other in the contact region and in a transition region that joins the contact region with the bulk of the shell, respectively. Fitting the f-d curve against Reissner's[23] linear law obtained a significantly larger Young's modulus, on the order of 300 MPa. It should be pointed out that in both the experimental studies that were mentioned earlier the shell thickness was treated as a known geometric parameter of the shell, and this facilitates parameter estimation significantly when it is unambiguously defined.

However, when coated microbubbles are interrogated, statically or acoustically, the shell thickness is not *a priori* known and more information is required in order to obtain reliable estimates of shell elasticity. In particular, Glynos *et al.*[25] measured Young's modulus of MBs covered with polymer polylactide with afm, using an independent formula for the shell thickness provided by the manufacturer of the MBs. The response of the obtained f-d curves is initially linear followed by a non-linear curved downwards regime in the manner obtained by Elsner *et al.*[22] for multilayer electrolyte shells. Reissner[23] and Pogorelov[24] have developed simple analytical models for the f-d relation for the pre and post-buckling stages which are very useful for the shell properties' characterization, see also Sec. IV of the present article. Combination of the transition from Reissner to Pogorelov regime can accurately calculate Young's modulus and the shell thickness without prior knowledge of the shell thickness,[26] treating the force exerted by the cantilever as a point load. More recently, Lytra *et al.*[27,28] extended the analytical expressions in order to account for the finite length of contact between the cantilever and the MB, instead of a point force that was originally assumed by Reissner and Pogorelov, with also reliable estimates of these two properties. Finally, Buchner Santos *et al.*[29] performed similar afm measurements for MBs covered with phospholipid monolayer (Definity). In this case, the response in f-d curves differs significantly from the previous case because an extensive linear regime is detected followed by a slightly curved upwards area. The latter part of the response curve cannot be associated with buckling. Rather, it signifies the influence of stretching in the bulk of the shell in the manner obtained previously by Lulevich *et al.*[20] also by performing afm measurements. It should be stressed, however, that resorting to the nonlinear model proposed by the latter study did not provide accurate estimates of shell elasticity, even when the shell thickness is known, for the statically interrogated shells.[29] Moreover, in that same study,[29] resorting to the Reissner model did not provide reliable estimates of the shell elastic modulus either. Nonetheless, the linear Reissner regime was present in afm measurements of lipid shells available in the literature.[30] As will be seen in the present study, proper combination of the linear Reissner regime with the nonlinear curved down or upwards regimes is required in order to provide reliable estimates of both types of shells without prior knowledge of the shell thickness. This is essential for treatment of lipid shells for which defining a shell thickness is not always possible, and using the area dilatation and bending resistance as the primary shell properties, instead of Young's modulus and shell thickness, constitutes the most appropriate shell model.[31]

In all of the above measurements, the coating behaves as an elastic shell under the forcing of a rigid cantilever and the equilibrium is reached due to internal tensions and moments developed by the shell. Therefore, it is a contact problem between the two bodies. In classic shell mechanics, the contact problem was originally studied by Hertz[32] for the contact of two curved bodies and relatively recently Johnson, Kendall, and Robert[33] (JKR model) extended Hertz's work to account for adhesion. More recently Shanahan[21] applied the above methodology to the case of an elastic membrane in an effort to obtain reliable estimates of its adhesion energy through the pull-off force from a flat rigid solid. In a different context, Seifert and Lipowsky introduced the concept of contact potential in order to study adhesion and stability of a vesicle onto a solid substrate.[34] However, due to the hydrophilic nature of the cantilever and these coatings, phospholipid shells, in particular, an ultrathin water film occupies the space between the MB and the cantilever and full contact is not possible. Thus, the shell is deformed subject to the disjoining pressure that develops in the liquid film. The latter is gradually thinning in response to the external forcing, and the resulting disjoining pressure is transferred to the deforming shell. The disjoining or Derjaguin pressure is a manifestation of short range forces such as London van der Waals interactions, electric double layers, or structural forces associated with the orientation of molecules that can be attractive or repulsive and tend to dominate other forces, such as Laplace pressure, in contact regions.[35,36] These forces can be collectively modeled in terms of a long range attractive and short range repulsive potential[37] that signifies the forces that emerge between the shell and cantilever as they approach each other and offers a convenient means to model the adhesion problem,[34,38] and the contact problem in general, via an interaction potential. In this fashion, use of the interaction potential has become a useful tool for the study of a variety of contact problems ranging from the study of adhesion and stability of vesicles on solid substrates[38,39] to wetting transitions of drops resting on patterned surfaces.[40] Thus a smooth distribution of the force that is exerted by the cantilever on the deforming shell can be obtained that can be used in order to capture the different response patterns observed in afm. A relevant study,[41] albeit in the absence of an external load, was conducted via an energy minimization principle in order to capture buckling transitions due to van der Waals adhesion of a spherical shell onto a rigid substrate. Despite the amount of effort dedicated to the study of static response of shells, see also Neubauer *et al.*[42] for a recent review article, there is lack in comprehensive modeling of their response in a manner that closely simulates atomic force microscopy measurements, especially in terms of providing an accurate description of the load distribution in different parametric ranges. Standard numerical methodologies do not provide the load distribution,[43,44] while more recent studies typically employ commercial packages[22,45,46] that do not place emphasis on the load distribution, thus compromising the ability to capture non-standard response patterns. To this end, in the present study, the static response of a coated microbubble that is symmetrically squeezed by two rigid plane surfaces is modeled in the above-described fashion that couples the elastic stresses that develop in the shell with the intermolecular forces that mediate the force exerted by the cantilever, through the disjoining pressure. Numerical simulations are performed with the finite element method using B-cubic splines as basis functions in order to accommodate the bending stresses that develop in the shell. Nonlinear elasticity is adopted[47] in order to model the in-plane and shear elastic tensions that develop on the shell, coupled with the linear Hooke's law and strain softening Mooney Rivlin constitutive law.[48] An extensive parametric study is conducted in order to ascertain the relative importance of different stiffness elements on the response and recover the patterns described earlier in the literature.

The rest of the paper is organized as follows: In Sec. II, the geometry and governing equations are presented, while the numerical methodology and benchmark calculations are presented in Sec. III. In Sec. IV, an asymptotic model is presented as a tool for categorizing the previously identified response patterns and validating the numerical results. A first attempt is also made to recover shell elastic properties by cross examining the numerical with the asymptotic results. In Sec. V, we present numerical results along with a parametric study for MBs covered with a polymeric (Sec. V A) and phospholipid (Sec. V B) shell in order to explain the relative influence of elastic properties and dimensionless numbers. Finally, the main findings and conclusions of the present paper are summarized in Sec. VI.

II. FORMULATION OF THE PROBLEM

A. Geometry and Lagrangian description

We consider an axisymmetric MB that is encapsulated by an elastic biomaterial (polymer or phospholipid monolayer), Fig. 1(a), and has a spherical stress free state. The generatrix of the full axisymmetric microbubble is represented by Lagrangian markers that are assigned to the independent variable ξ, $\xi \in [0, 1]$. Upon introducing variable ξ, it is possible to describe complex shapes of the interface with the spherical coordinates of each marker written as functions of ξ,

$$r = r(\xi) \quad \text{and} \quad \theta = \theta(\xi), \quad \forall \xi \in [0, 1]. \tag{1}$$

Moreover, the normal and tangential vectors of an arbitrary point are[49]

$$\vec{n} = \frac{r\theta_\xi \vec{e}_r - r_\xi \vec{e}_\theta}{s_\xi}, \ \vec{t}_s = \frac{r_\xi \vec{e}_r + r\theta_\xi \vec{e}_\theta}{s_\xi}, \ \text{and} \ \vec{t}_\varphi = r \sin\theta \vec{e}_\varphi, \tag{2}$$

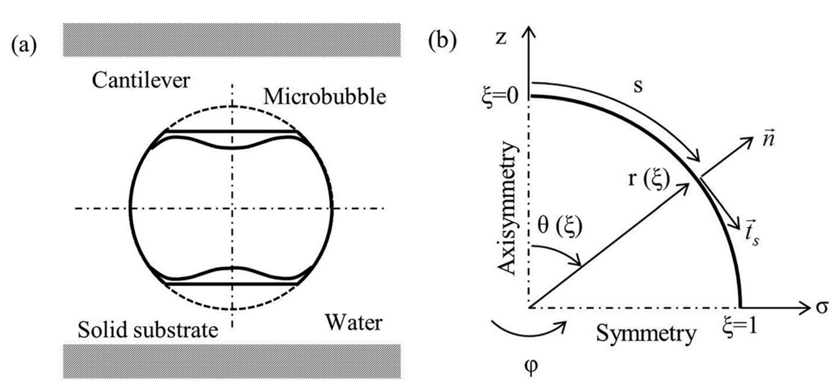

FIG. 1. (a) Schematic representation of a microbubble under the cantilever resting on a similar solid substrate, with dashed and solid lines denoting the undeformed and deformed (flat and buckling) configurations, respectively; (b) the Lagrangian description of the generatrix with a certain value of variable ξ assigned to each Lagrangian marker. $\xi = \theta_0/(\pi/2)$, where θ_0 denotes the azimuthal position of the markers at the spherical stress free reference state, (r, θ, φ) are the spherical coordinates of each marker in deformed configuration, s is the arc-length, $\vec{n}, \vec{t}_s$ are the unit normal and tangential vectors, and (σ, z) are the radial and axial coordinates of the cylindrical coordinated system, $\sigma = r\sin\theta$, with the same origin as the above spherical coordinate system.

where $\vec{e}_r, \vec{e}_\theta, \vec{e}_\varphi$ denote the unit vectors of a spherical coordinate system and s denotes the arc-length across the generatrix, $s_\xi = ds/d\xi = \left(r^2\theta_\xi^2 + r_\xi^2\right)^{0.5}$; ξ signifies differentiation when it is used as subscript. We assume that the MB rests on a plane surface of similar nature as the cantilever and consequently undergoes symmetric deformations with respect to the equator as it is compressed by the latter. In this fashion, the substrate exerts an equal but opposing force to the shell, with respect to that of the cantilever, and symmetry is satisfied. As will be seen in the following, this assumption does not restrict in any way the validity of the simulations, in comparison with measurements obtained in the same parameter range, provided that shell deformation does not become exceedingly severe to the extent that three dimensional wrinkling is avoided. Thus the physical domain of our analysis extends in $\theta \in [0, \pi/2]$, see also Fig. 1(b); $\xi \equiv \theta_0/(\pi/2)$ with θ_0 denoting the azimuthal position of the marker points at the spherical stress free reference state.

The curvature tensor of the interface is defined as

$$\underline{\underline{B}} = \vec{\nabla}_s \vec{n}, \tag{3}$$

and the principal curvatures along the meridional (or azimuthal) s and polar φ directions, and the corresponding mean curvature, assume the form

$$k_1 = k_s = \frac{r_\xi^2\theta_\xi + r\left(r_\xi\theta_{\xi\xi} - r_{\xi\xi}\theta_\xi\right)}{s_\xi^3} + \frac{\theta_\xi}{s_\xi} = \frac{1}{r_s}, \tag{4a}$$

$$k_2 = k_\varphi = \frac{\theta_\xi}{s_\xi} - \frac{r_\xi \cot\theta}{r s_\xi} = \frac{1}{r_\varphi}, \tag{4b}$$

$$2k_m = k_s + k_\varphi. \tag{4c}$$

B. Elastic tensions and moments

The MB is covered by a biocompatible material, usually phospholipid monolayer or polymer, in order to decelerate gas diffusion in water or blood. The encapsulation provides also mechanical strength. Thus the MB is possible to withstand external forces by developing elastic tensions and moments. In the present paper, we describe the elastic tensions and moments in the context of the theory of thin elastic shells and continuum mechanics.[47] In the elastic shell, in-plane and shear tensions along with bending moments are developed as a result of deformation of the shell subject to an external load. In Fig. 2, the tensions and moments are illustrated on an axisymmetric surface patch that is assumed to undergo axisymmetric deformations. As can be gleaned from the above figure, both tensions and moments are written in the curvilinear [s, φ, n] system for simplicity since the [s, φ] coordinates coincide with the principal directions[50,51] of strain in the context of axisymmetry. Therefore, the meridional (τ_{ss}) and polar ($\tau_{\varphi\varphi}$) tensions are introduced, which correspond to the in-plane stress resultants. The transverse shear stress q lies in an s-φ plane and arises as a result of the variation of the meridional (m_{ss}) and polar ($m_{\varphi\varphi}$) bending moments on the shell interface. The total tension tensor and bending moment tensor read as

$$\underline{\underline{T}} = \tau_{ss}\vec{t}_s\vec{t}_s + \tau_{\varphi\varphi}\vec{t}_\varphi\vec{t}_\varphi + q\vec{t}_s\vec{n} \quad \text{and} \quad \underline{\underline{m}} = m_{ss}\vec{t}_s\vec{t}_s + m_{\varphi\varphi}\vec{t}_\varphi\vec{t}_\varphi. \tag{5}$$

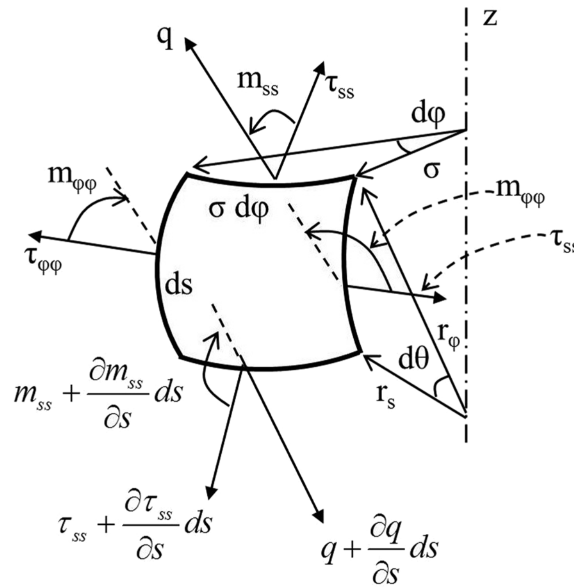

FIG. 2. Elastic in-plane (τ_{ss} and $\tau_{\varphi\varphi}$) and shear (q) tensions, along with bending moments (m_{ss} and $m_{\varphi\varphi}$) acting on an axisymmetric infinitesimal surface patch on a sphere with dimensions ds × (σdφ).

A large number of elastic materials respond linearly in the presence of an external load for small deformations.[48,50] However, with further increase in the load, the f-d relation may become non-linear, even if buckling or other phenomena do not occur. In this case, their behavior is characterized as strain softening or strain hardening, depending on the variation of the effective elasticity modulus. The strain softening materials exhibit a smaller elasticity modulus as the deformation increases, while the opposite happens for strain hardening materials. These observations can be described mathematically using the appropriate constitutive law. For the first group of materials, Hook's law is more relevant, while for the strain softening and strain hardening materials Mooney-Rivlin and Skalak constitutive laws are used,[31,48,50] respectively. They are all associated with the appropriate form of energy per unit of undeformed surface w. In the following, the strain energy function of Hooke's law, w^{HK}, and Mooney-Rivlin constitutive law, w^{MR},

$$w^{HK} = \frac{G_s}{4(1-\nu)}\Big[\left(\lambda_s^2 - 1\right)^2 + 2\nu\left(\lambda_s^2 - 1\right)\left(\lambda_\varphi^2 - 1\right) + \left(\lambda_\varphi^2 - 1\right)^2\Big], \tag{6a}$$

$$w^{MR} = w(I_1, I_2) = \frac{G_{MR}}{2}\left[(1-b)\left(I_1 + 2 + \frac{1}{I_2+1}\right) + b\left(\frac{I_1+2}{I_2+1} + I_2 + 1\right)\right], \tag{6b}$$

are mostly used, with

$$\lambda_s = \frac{ds}{ds^{SF}} = \frac{\sqrt{r_\xi^2 + r^2\theta_\xi^2}}{r^{SF}\theta_\xi^{SF} = R_0\pi/2}, \quad \lambda_\varphi = \frac{\sigma d\varphi}{(\sigma d\varphi)^{SF}} = \frac{\sigma}{\sigma^{SF}}, \tag{7a}$$

$$I_1 = \lambda_s^2 + \lambda_\varphi^2 - 2, \quad I_2 = \lambda_s^2\lambda_\varphi^2 - 1 \tag{7b}$$

denoting the principal stretch ratios and 2d invariants of the Green-Lagrange deformation tensor, defined on the deformed shell; $\sigma = r\sin\theta$ is the radial polar coordinate while ν signifies the Poisson ratio. Upon introducing the variation of strain energy, the in-plane tensions assume the following form in the meridional and polar directions:

$$\tau_{ss}^{HK} = \frac{G_s}{\lambda_\varphi(1-\nu)}\left[\lambda_s^2 - 1 + \nu\left(\lambda_\varphi^2 - 1\right)\right],$$
$$\tau_{\phi\phi}^{HK} = \frac{G_s}{\lambda_s(1-\nu)}\left[\lambda_\phi^2 - 1 + \nu\left(\lambda_s^2 - 1\right)\right], \tag{8a}$$

$$\tau_{ss}^{MR} = \frac{G_{MR}}{\lambda_s\lambda_\varphi}\left[\lambda_s^2 - \frac{1}{\left(\lambda_s\lambda_\varphi\right)^2}\right]\left[1 + b\left(\lambda_\varphi^2 - 1\right)\right],$$
$$\tau_{\phi\phi}^{MR} = \frac{G_{MR}}{\lambda_s\lambda_\varphi}\left[\lambda_\phi^2 - \frac{1}{\left(\lambda_s\lambda_\varphi\right)^2}\right]\left[1 + b\left(\lambda_s^2 - 1\right)\right], \tag{8b}$$

where $G_s = \chi/(2(1+\nu))$, $G_{MR} = \chi/3$ denote the surface shear modulus and χ denotes the area dilatation modulus. $\chi = Eh = 3Gh$, with E and G denoting the 3D Young's modulus and shear modulus, respectively, and b denotes a dimensionless parameter, $b \in [0, 1]$, defining the extent of nonlinearity of the Mooney-Rivlin law. The case $b = 0$ corresponds to a neo-Hookean membrane, whereas as b tends to zero the membrane becomes softer.[48] Moreover, the description of the strain softening behavior with the Mooney-Rivlin constitutive law allows for unlimited dilatation of the membrane that is satisfied by progressive membrane thinning. More details on the derivation and interpretation of the different constitutive laws that provide the in-plane tensions are provided elsewhere in the literature.[48,50,51]

A standard quadratic function is employed for the bending energy of the shell,[52]

$$w_b = \frac{k_b}{2}\left(K_s^2 + 2\nu K_s K_\varphi + K_\varphi^2\right), \tag{9}$$

where $K_i = \lambda_i k_i - k_i^{SF}$ are the bending strains along the principal directions s and φ, ($i \to s$ or φ and indices are not summed) while for an initially spherical microbubble $k_i^{SF} = 1$. Employing the first variation of the bending energy with respect to the bending strain[52,53] provides the bending moments in a similar fashion to the in-plane elastic tensions,

$$m_{ss} = \frac{1}{\lambda_\varphi}\frac{\partial w_b}{\partial K_s} = \frac{k_b}{\lambda_\varphi}\left(K_s + \nu K_\varphi\right),$$
$$m_{\varphi\varphi} = \frac{1}{\lambda_s}\frac{\partial w_b}{\partial K_\varphi} = \frac{k_b}{\lambda_s}\left(K_\varphi + \nu K_s\right), \tag{10}$$

where k_b denotes the bending modulus that, according to classical shell theory,[47] reads as

$$k_b = \frac{Eh^3}{12\left(1-\nu^2\right)}. \tag{11}$$

It should also be noted that MBs that are covered with polymer are stiff in terms of their Young's modulus ($E \sim$ GPa); their shell thickness is relatively large ($h \sim$ 10-40 nm), and consequently, it can be concluded that their bending modulus follows the above relation with Young's modulus and the shell thickness (h), as in convectional shells. On the other hand, MBs that are covered with the phospholipid monolayer are generally less stiff, whereas their shell thickness cannot be easily defined. Therefore, in the present study, it is assumed that for MBs covered with polymer the independent elastic properties are Young's modulus (E) and the shell thickness (h), whereas for phospholipid coating the independent properties are the area dilatation modulus (χ) and the bending modulus (k_b). Finally the elastic shear tension is related to the bending moments via a moment balance on an infinitesimal surface patch,[50,54]

$$\vec{q} = \vec{\nabla}_s \cdot \underline{\underline{m}} \cdot \left(\underline{\underline{I}} - \vec{n}\vec{n}\right). \tag{12}$$

C. Equations of equilibrium

In order to simulate actual afm measurements that take place in an aqueous solution, the microbubble is considered to be emerged in a liquid phase with the cantilever positioned in its vicinity and gradually squeezing it, Fig. 3(a). In this fashion, the evolution of the static equilibrium of the microbubble is investigated at different stations of the cantilever characterized by the distance z_0 between it and the center of mass of the shell, Fig. 3(a). The latter, in view of the symmetry of the problem, is positioned at the intersection between the two axes of symmetry, i.e., the axis of rotation z and the mid plane between the two rigid surfaces squeezing the microbubble, Fig. 3(a). In this process, due to the hydrophilic nature of the shell and the cantilever, an ultrathin water layer with height $\delta = \delta(\xi)$ occupies the space between them that resists

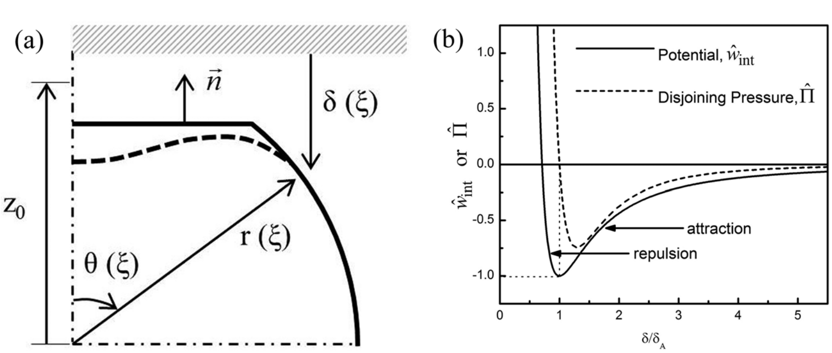

FIG. 3. (a) Schematic representation of a microbubble deformed by a flat and rigid cantilever. As the cantilever approaches, i.e., z_0 decreases, the applied force on the shell increases and, depending on the elastic parameters, flattened or buckled shapes arise. (b) Dimensionless potential, $\hat{w}_{int} = w_{int}(\delta)/w_0$, and dimensionless disjoining pressure, $\hat{\Pi} = \Pi(\delta)\,\delta_A/w_0$, as a function of the relative distance from the cantilever, δ/δ_A.

thinning as the force exerted by the cantilever increases, Fig. 3(b). This constitutes an additional resistance to the cantilever's advancement which is modeled as an additional pressure of the water near the contact area in comparison with the bulk aqueous phase. This pressure difference is the sum of intermolecular forces that act between the water film and the shell, and it is known as disjoining pressure. This concept is employed in the present study for the description of the interaction between the cantilever and the shell, by introducing a long range attractive-short range repulsive potential function. A typical form of the interaction potential[37–39] is

$$w_{Int}(\delta) = w_0\left[\left(\frac{\delta_A}{\delta}\right)^4 - 2\left(\frac{\delta_A}{\delta}\right)^2\right], \tag{13a}$$

$$W_{Int} = \int_A w_{Int} dA \xrightarrow{Symmetry} W_{Int} = 2\pi 2\int_0^1 w_{Int} r \sin\theta \frac{ds}{d\xi} d\xi, \tag{13b}$$

$$\delta(\xi) = z(\xi) - z_0, \tag{13c}$$

where $\hat{z}_0$ denotes the relative position of the cantilever with respect to the equatorial plane of the MB, Fig. 3(a), and δ_A denotes the characteristic length for which the interaction potential takes the minimum negative value $-w_0$, Fig. 3(b). Note also that in Fig. 3(b) a positive (repulsive) force on the shell is taken to point away from the cantilever. As the distance between the cantilever and shell decreases and approaches the characteristic length δ_A, an additional source of energy is attributed to the shell interface, W_{Int}, reflecting its interaction with the cantilever. The total energy content of the shell, provided by the sum of strain, bending, intermolecular, gas compression, and surface energy, reads as

$$U_T = W_{str} + W_b + W_{int} + W_c + W_s, \tag{14}$$

where

$$W_{str} = \int_A w_{str} dA, \quad \text{with} \quad w_{str} = w^{HK} \text{ or } w^{MR}, \tag{15a}$$

$$W_b = \int_A w_b dA = \int_A \frac{k_b}{2}\left(K_s^2 + 2\nu K_s K_\varphi + K_\varphi^2\right) dA, \tag{15b}$$

$$W_c = -\int_{V_0}^{V} (P_G - P_0)\, dV \xrightarrow{P_0 = P_A} W_c = P_A(V - V_0) - \frac{P_A V_0}{1-\gamma}\left(\left(\frac{V_0}{V}\right)^{\gamma-1} - 1\right), \tag{15c}$$

$$W_s = \int_A \gamma_{BW} dA, \tag{15d}$$

$$W_{int} = \int_A w_{\text{int}}(\delta)\, dA. \tag{15e}$$

In the above, P_A denotes the ambient atmospheric pressure, P_0, V_0 and P_G, V denote the internal gas pressure and volume at stress free conditions and at static equilibrium subject to deformation, respectively, and γ and γ_{BW} denote the polytropic gas constant and shell-water interfacial tension.

Minimization of the total energy gives the force balance in the normal and tangential directions,

$$\vec{n}: P_G - P_A + \Pi = k_s\tau_{ss} + k_\varphi\tau_{\varphi\varphi} + 2k_m(\gamma_{BW} + w_{\text{int}}) - \frac{1}{\sigma}\frac{\partial(\sigma q)}{\partial s}, \tag{16a}$$

$$\vec{t}_s: -\left[\frac{\partial\tau_{ss}}{\partial s} + \frac{1}{\sigma}\frac{\partial\sigma}{\partial s}\left(\tau_{ss} - \tau_{\varphi\varphi}\right) + k_s q\right] = 0, \tag{16b}$$

while the elastic shear tension, based on the bending moment balance in Eq. (12), reads

$$q = \frac{1}{\sigma}\frac{\partial\sigma}{\partial s}\left[\frac{\partial(\sigma m_{ss})}{\partial\sigma} - m_{\varphi\varphi}\right]. \tag{16c}$$

The disjoining pressure Π arises as part of the minimization of the intermolecular energy with respect to the radial, r, and azimuthal, θ, position of the shell and equals the derivative of the interaction potential in the normal direction,

$$\Pi = -\frac{\partial w_{\text{int}}}{\partial n} = \frac{4w_0}{\delta_A}\left[\left(\frac{\delta_A}{\delta}\right)^5 - \left(\frac{\delta_A}{\delta}\right)^3\right]\frac{\partial\delta}{\partial n} \xrightarrow[\delta = z_0 - z]{\vec{n} = \sigma_s\vec{e}_z - z_s\vec{e}_\sigma} \Pi = -\frac{4w_0}{\delta_A}\left[\left(\frac{\delta_A}{\delta}\right)^5 - \left(\frac{\delta_A}{\delta}\right)^3\right]\sigma_s, \tag{17}$$

whereas the total intermolecular force on the shell is

$$\vec{F} = -\frac{\delta W_{Int}}{\delta\vec{r}} = \int_A \left(-\frac{\partial w_{\text{int}}}{\partial n} - 2k_m w_{\text{int}}\right)\vec{n}\, dA. \tag{18}$$

More details on the derivation of the disjoining pressure Π and the total normal component of the intermolecular forces on the shell, $\Pi - 2k_m w_{\text{int}}$, via the minimization of the integral in Eq. (15e) are provided in the Appendix. The second term, $2k_m w_{\text{int}}$, in the integrand of Eq. (18) is typically subdominant to the disjoining pressure. It should also be stressed that in the above derivation the normal vector points toward the cantilever and $d\delta/dn < 0$, see also Fig. 3(a). As a result, attraction/repulsion on the shell is signified by a positive/negative disjoining pressure Π, contrary to standard representations such as the one shown in Fig. 3(b) for which the normal to the interface is taken to point away from the substrate and positive Π values denote repulsion. The formulation in Eq. (16) adopts the convention used for the derivation of Eq. (18). Nonetheless, graphic representations of the force on the shell shown in Secs. III–V adopt the convention in Fig. 3(b) for conformity with the literature.

Regarding the nature of the force, as the minimum distance, δ, between any point on the shell and cantilever increases ($\delta \gg \delta_A$), the potential is essentially zero and no significant interaction between the shell and cantilever is registered. As the cantilever approaches the shell, in other words, as the distance z_0 from the shell equator decreases, δ typically decreases as well while the interaction potential acquires a decreasing negative value ($\delta \sim \delta_A$). Therefore, when attractive forces prevail in this regime, i.e., $\delta > \delta_A$, the disjoining pressure and the resulting force acquire a positive value in Eq. (16a) and along with the gas pressure push the shell toward the cantilever. At

$\delta = \delta_A$, the potential has a minimum value ($-w_0$); this is the position where the disjoining pressure and the force vanish, and with further decrease in distance between them ($\delta < \delta_A$), the two points are in repulsion and consequently the disjoining pressure and the resulting force change sign becoming negative. In the present study, both potential and disjoining pressure have a distribution along the shell surface since the liquid film height, $\delta(\xi)$, is not generally constant. Thus, the total force becomes zero at a position slightly different from the characteristic length δ_A. In particular, it is a position where a part of the shell is in repulsion, usually the area around the contact region, while the rest of the shell is in attraction. In fact, at a certain distance z_0, the overall force exerted by the cantilever on the shell vanishes as a result of the repulsion in the contact region and attraction in the rest of the shell counteracting each other. At this reference point, we set the deformation Δ to zero and we calculate subsequent deformations via the following transformation in dimensionless form:

$$\hat{d} = \Delta/R_0 = \hat{z}_0\,(F = 0) - \hat{z}_0\,(F). \tag{19}$$

Provided the interaction between the shell and cantilever is relatively weak, $w_0/\chi \ll 1$, so that multiple crossings of the horizontal axis that measures the interaction force do not occur in the f-d curve and the MB remains mostly spherical when this force vanishes, the above is a practical way to measure deformation. It essentially captures the cantilever's movement, and it is the same as the deformation of the shell pole in the regime of flat shapes, while in the regime of buckled shapes it is the same as the deformation of the ring at the dimple area. In addition, it must be pointed out that we adopt this approach because we wish to compare against the afm experimental data in a future study. The above are clearly illustrated in Sec. V, where the force and the deformed shape are calculated as part of the post-processing of the simulation.

In addition, the reduction of the shell volume during compression is associated with pressure variations of the encapsulated gas via the isothermal gas law,

$$P_G V^{\gamma} = P_0 V_0^{\gamma}, \tag{20a}$$

$$V = \int_V dV = \frac{4\pi}{3}\int_0^1 r^3\theta_\xi \, \sin\,\theta d\xi, \tag{20b}$$

where subscript 0 denotes the pressure and the volume in the reference state, i.e., $P_0 = P_A + 2\gamma_{BW}/R_0$, $V_0 = 4\pi R_0^3/3$, and $\gamma = 1.07$. The reference state is typically spherical and stress-free unless otherwise stated.

The problem formulation is rendered dimensionless by introducing the stress free radius as the characteristic length scale, R_0. Then the solution depends mainly on the following dimensionless parameters, namely, $\hat{k}_b$, $\hat{P}_A$, $\hat{\gamma}_{BW}$, $\hat{W}_0$, and $\hat{z}_0$:

$$\hat{k}_b = \frac{k_b}{\chi R_0^2}, \quad \hat{P}_A = \frac{P_A R_0}{\chi}, \quad \hat{\gamma}_{BW} = \frac{\gamma_{BW}}{\chi},$$
$$\hat{W}_0 = \frac{w_0}{\chi}, \quad \hat{z}_0 = \frac{z_0}{R_0}, \quad \hat{\chi} = 1, \tag{21a}$$

measuring the relative stiffens of bending, gas compressibility, surface tension, and interaction potential with respect to the resistance to elongation. $\hat{z}_0$ represents the dimensionless distance between the cantilever and the equatorial plane of symmetry of the microbubble that is located midway between the cantilever and rigid substrate. It is used as a parameter that controls the translation of the cantilever with respect to the shell and implicitly provides a means to gradually increase the force exerted on the shell, as this is calculated via Eq. (18). For polymeric shells that normally have thicker coatings, bending resistance is related to the elastic modulus and the shell thickness,[47]

$$\hat{k}_b = \frac{k_b}{\chi R_0^2} = \frac{\frac{Eh^3}{12(1-\nu^2)}}{EhR_0^2} = \frac{1}{12\,(1-\nu^2)}\left(\frac{h}{R_0}\right)^2. \tag{21b}$$

We apply boundary conditions of axisymmetry in the pole, $\xi = 0$, and symmetry in the equator, $\xi = 1$,

$$r_\xi = 0 \quad \text{at } \xi = 0 \text{ and } 1, \tag{22a}$$

$$\theta_{\xi\xi} = 0 \quad \text{at } \xi = 0 \text{ and } 1, \tag{22b}$$

$$\theta\,(\xi = 0) = 0 \quad \text{and} \quad \theta\,(\xi = 1) = \frac{\pi}{2}. \tag{22c}$$

Finally, in the graphs shown in Secs. III–V, the disjoining pressure Π, the total energy U_T, its components W_i, the force, and the deformation are made dimensionless as follows:

$$\hat{\Pi} = \frac{\Pi\delta_A}{w_0}, \quad \hat{U}_T = \frac{U_T}{\chi R_0^2}, \quad \hat{W}_i = \frac{W_i}{\chi R_0^2},$$
$$\hat{F} = \frac{F}{\sqrt{\chi k_b}}, \quad \hat{z}_0 = \frac{z_0}{R_0}. \tag{23}$$

III. NUMERICAL IMPLEMENTATION AND VALIDATION

A. Finite element method

Modeling of the elasticity terms for thin shells with finite thickness requires the mathematical description of the first derivative of shear tension. Therefore the equilibrium equations contain high order derivatives. In particular, the normal force balance contains fourth order derivatives of the r and θ coordinates and the tangential force balance contains their third derivative. As a result, we use the b-cubic splines, which are piecewise cubic curves[55] for the representation of the unknown position of the shell. The unknown shell coordinates r and θ are written as

$$r\,(\xi) = \sum_{j=0}^{N+1} a_j B_j \quad \text{and} \quad \theta\,(\xi) = \sum_{j=0}^{N+1} b_j B_j, \tag{24}$$

where α_j and b_j are the unknown coefficients, B_j are the spline basis functions, and N is the total node number. The spline representation introduces two additional coefficients, which correspond to the imaginary nodes $j = 0$ and $N + 1$, and they are calculated by the imposition of the boundary conditions. In order to solve the above set of non-linear equations (16) and (20) along with boundary conditions (22), we use the Galerkin finite element method. Thus, integrating by parts twice the normal force balance, we reduce the order of the differential equation while b-cubic splines guarantee continuity up to the second derivative.[55] In the same manner, upon a single integration by parts of the tangential force balance, we eliminate the derivative of the in-plane tension, τ_{ss}, and the shear tension, q. Thus, by integrating over the deformed shell surface, $dA = r\sin\theta d\varphi ds$, the weak form of the problem formulation reads as

$$R_1 = \int_0^1 \Big[\Big(k_s\tau_{ss} + k_\varphi\tau_{\varphi\varphi} + 2k_m\left(\gamma_{BW} + w_{\text{int}}\right) - P_G + P_A - \Pi\Big) B_i\sigma s_\xi\Big]\, d\xi - \int_0^1 \left[\frac{\sigma\left(B_{i,\xi\xi}s_\xi - B_{i,\xi}s_{\xi\xi}\right)}{s_\xi^2} + \frac{m_{\varphi\varphi}B_{\iota,\xi}\sigma_\xi}{s_\xi}\right] d\xi + \left\{\frac{\sigma m_{ss}B_{i,\xi}}{s_\xi} - \sigma q B_i\right\}_{\xi=0}^{\xi=1} = 0, \tag{25a}$$

$$R_2 = \int_0^1 \Big[\tau_{ss}B_{i,\xi}\sigma + B_i\sigma_\xi\tau_{\varphi\varphi} + \sigma m_{ss}\left(k_{s,\xi}B_i + k_sB_{i,\xi}\right) + k_sm_{\varphi\varphi}B_i\sigma_\xi\Big]\, d\xi - \left\{\left(k_sm_{ss} + \tau_{ss}\right)\sigma B_i\right\}_{\xi=0}^{\xi=1} = 0, \tag{25b}$$

$$R_3 = P_GV^\gamma - P_0V_0^\gamma = 0. \tag{25c}$$

The boundary terms in curly brackets result from the integration by parts; they are zero at $\xi = 0$ since $\sigma(\xi = 0) = 0$ and take a non-zero value at $\xi = 1$, thereby modifying the last three equations of normal and tangential force balance. Integration along the polar φ-direction is eliminated due to the assumption of axisymmetry. The above relations constitute a non-linear set of equations, $\vec{R}\left(\vec{x}\right) = \vec{0}$, that we solve with the standard Newton-Rapshon method,

$$\underline{\underline{J}}\left(\vec{x}^{n+1}\right)\cdot\left(\vec{x}^{n+1} - \vec{x}^{n}\right) = -\vec{R}\left(\vec{x}^{n+1}\right), \tag{26}$$

where $\vec{R}\left(\vec{x}\right)$ is the vector of residuals, $\underline{\underline{J}} \equiv \partial R_i/\partial x_j$ signifies the Jacobian matrix and $\vec{x}$ denotes the unknown vector, $\vec{x} = [a_0, b_0, \ldots, a_i, b_i, \ldots, a_{N+1}, b_{N+1}, P_G]^{\mathrm{T}}$. The Jacobian matrix is in arrow form, thus significantly reducing the time required to invert the matrix during Newton's iterations. Moreover, analytic calculation of the Jacobian matrix ensures quadratic convergence of the solution. In addition, we seek different solutions as the relative position, $\hat{z}_0$, is reduced. We perform arc-length continuation to follow the solution around limit points,[53] beyond which a solution cannot be obtained as the operating parameter, $\hat{z}_0$, varies. In this case, parameter $\hat{z}_0$ is no longer known but is calculated as part of the solution. The stability of a certain solution branch is determined by the number of negative eigenvalues[56] for each one of the converged solutions obtained by varying the relative position $\hat{z}_0$.

B. Benchmark calculations

In order to validate our finite element methodology, we compare our results with simulations of the contact problem available from the literature. In particular, Updike and Kalnins[43,44] solved a similar problem in the context of conventional shell mechanics and calculated the f-d curve[43] and pressure distribution[44] between the shell and the flat punch assuming a linear material and small deformations. They found that most of the pressure is applied at the end of the contact region, in the sense that it can be replaced by a point force concentrated at the edge. In the latter studies, the response of the shell is described by the intersection of two solution branches in the f-d diagram. The first is the trivial solution pertaining to the linear part of the response that is characterized by flat shapes in the contact region, while the second branch of buckled shapes emerges as a bifurcation from the main one and is characterized by non-linear response, as will be discussed in Secs. IV and V.

Upon employing the formulation proposed by Updike and Kalnins,[44] the load distribution was indeed calculated[53] in agreement with results reported in the former study. This verified the tendency to produce an almost point load distribution with the peak located at the edge of the contact region, as the intensity of the load increases toward the buckling range. It was, however, difficult to obtain convergence with mesh refinement, especially as the angle that defines the contact region increases toward the buckling regime. In fact, the latter regime could not be captured in this fashion. As an alternative approach, we set the point load, Q_L in N/m, applied at the edge of the contact region, $\xi_L = \alpha/(\pi/2)$, and the normal force balance and kinematic condition are reformulated as follows:

$$P\left(\xi\right) = \delta\left(\xi_L\right)P_L \Rightarrow F = \int_A \delta\left(\xi_L\right)P_L dA = Q_L 2\pi\sigma_L, \tag{27a}$$

$$R_1 = \int_0^1 \Big[\Big(k_s\tau_{ss} + k_\varphi\tau_{\varphi\varphi} + 2k_m\gamma_{BW} + P_A - P_G\Big)B_i\sigma s_\xi\Big]\, d\xi - \int_0^1 \left[\frac{\sigma\left(B_{i,\xi\xi}s_\xi - B_{i,\xi}s_{\xi\xi}\right)}{s_\xi^2} + \frac{m_{\varphi\varphi}B_{i,\xi}\sigma_\xi}{s_\xi}\right] d\xi + \left[\frac{\sigma m_{ss}B_{i,\xi}}{s_\xi} - \sigma q B_i\right]_{\xi=0}^{\xi=1} + \sigma Q_L B_i\big|_{\xi=\xi_L} = 0 \quad i = 1,\ldots N, \tag{27b}$$

$$R_4 = z_\xi = r_\xi\,\cos\,\theta - r\theta_\xi\,\sin\,\theta = 0 \quad \text{at } \xi_L = \frac{\alpha}{\pi/2}. \tag{27c}$$

The unknown point load Q_L is introduced in the form of a discontinuity at the edge of the contact region, and residual R_2 corresponding to the tangential force balance is not modified in the above context. The parameters that are used in this simulation are the same as the ones employed in the literature;[43,44,57] $E = 10^9$ Pa, $R_0/h = 100$ (e.g., $R_0 = 10^{-7}$ m and $h = 10^{-9}$ m), $\nu = 0.3$, $\gamma_{BW} = 0$ N/m, and $\gamma = 0$, for a Hookean shell without pre-stress or interfacial tension. Parameter γ that controls the pressure variation is set to zero in order to maintain a fixed internal pressure as in the above studies. As can be gleaned from Fig. 4, our numerical results, obtained with a mesh of 400 B-cubic splines along the meridional direction, fully recover the analytical/numerical results provided in Refs. 43, 44, and 57 for both flat and buckling curves. In particular, as can be surmised by cross-examining panels (4a) and (4b), the f-d curves shown in Fig. 4(a), obtained using the modified formulation in Eqs. (27), exhibit the initial linear part known as Reissner regime followed by a nonlinear response pattern, $f \sim d^{1/2}$, known as the Pogorelov regime. Furthermore, the corresponding transition from shapes that are flattened around the pole region to shapes characterized by crater formation in the north pole region is captured, followed by a narrow bending strip where contact takes place before the shell regains its sphericity in the bulk. Eigenvalue calculations indicate the loss of stability of the Reissner regime at $d/h \sim 3$, which is very close to the value and corresponding angle of $10°$ available in the literature[57] that constitutes a bifurcation point in the standard calculation via Eqs. (27). This is a supercritical bifurcation that evolves into the branch with buckled shapes which inherits the stability of the main branch of flat shapes and whose energy content is lower than that of the main branch for the same relative deformation, see also Fig. 4(c). Please note that solely for the purpose of comparison with the work of Updike and Kalnins[43,44,57] the f-d axes in Fig. 4(a) are dimensionlized as $\hat{F} = 10^6 F/(2\pi E h R_0)$ and $\hat{d} = \Delta/h$.

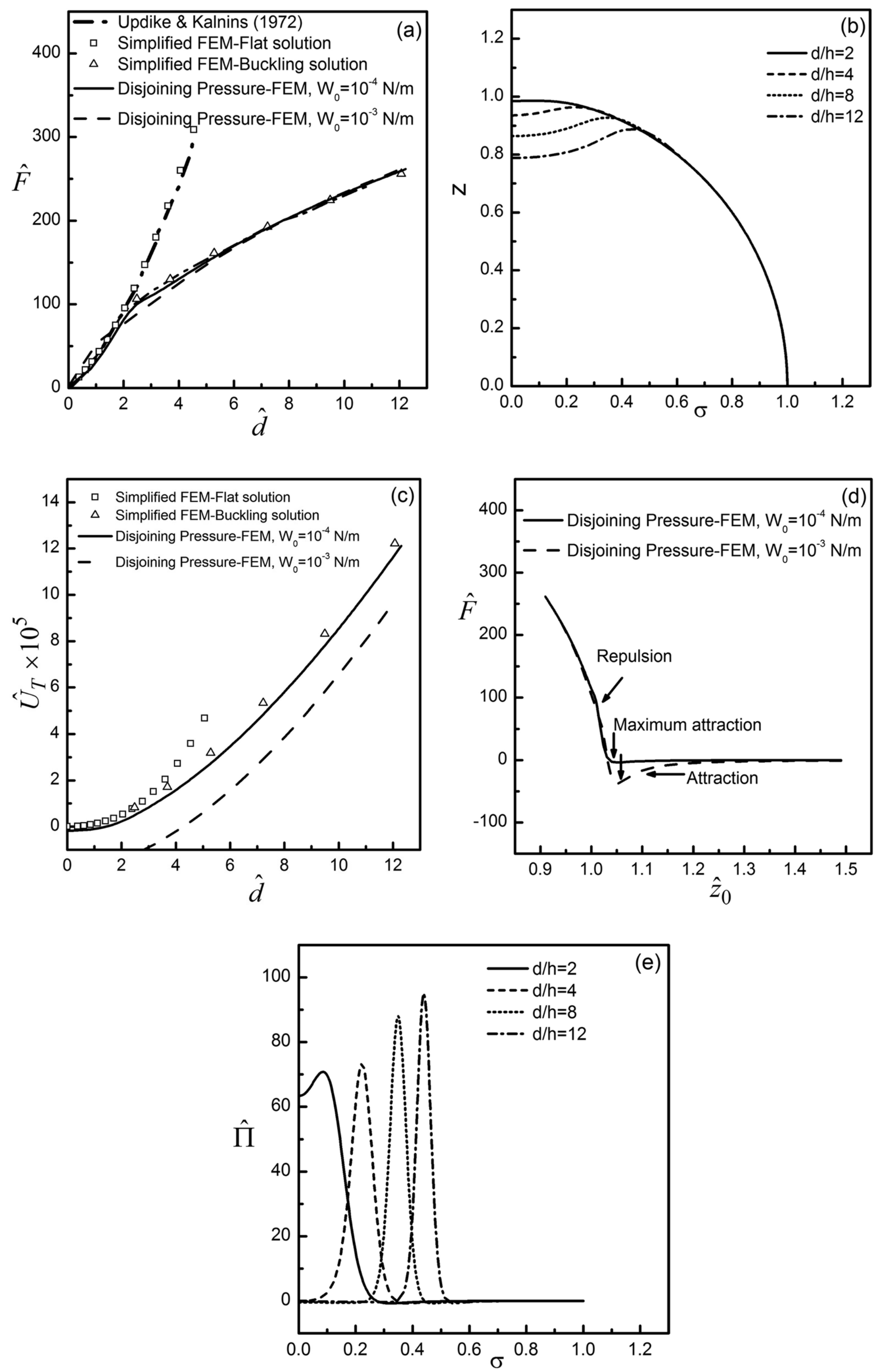

FIG. 4. (a) Comparison of dimensionless force $\hat{F}$as a function of dimensionless deformation $\hat{d}$ between the Updike and Kalnins[43,44,57] solution, the simplified model, and the intermolecular forces model for two different adhesive parameters (w_0), (b) MB in the deformed flat and buckling configuration obtained with the intermolecular forces model ($w_0 = 10^{-4}$ N/m), (c) dimensionless total energy $\hat{U}_T$ as a function of deformation $\hat{d}$, (d) comparison of force $\hat{F}$ as a function of dimensionless distance $\hat{z}_0$ between the two intermolecular forces model cases, (e) evolution of the dimensionless disjoining pressure distribution $\hat{\Pi}$ as a function of the radial coordinate σ for indicative values of deformation obtained with the intermolecular forces model ($w_0 = 10^{-4}$ N/m).

The above simulations were repeated with the novel formulation presented herein involving the intermolecular forces, see also Eq. (16). The benchmark calculations as well as results presented in Secs. IV and V were obtained with a 400 element mesh of B-cubic splines. Mesh refinement simulations to 400 and 800 elements fully recover the load distribution, contrary to the standard formulation[44] that had problems in achieving satisfactory numerical convergence, especially at large deformations. Figure 4(d) illustrates the total dimensionless force from the latter simulations plotted against the distance between the cantilever and shell equator, $\hat{z}_0$, with marked areas of overall attraction and repulsion. Selecting a relatively weak interaction potential, $w_0 = 10^{-4}$ N/m, and a typical value for the characteristic range of the intermolecular forces, $\delta_A = 50$ nm, we obtain the standard response pattern available in the literature[43,44,57] and recovered with the simplified formulation provided by Eq. (26), for the compression of a spherical shell by two rigid plane surfaces. Thus, the validity of our methodology was verified, see also panels (4a)–(4c). The above value for the interaction potential was selected, in the absence of any experimental data, so that we recover the numerical results from the literature. Using a stronger interaction potential gives rise to limit points in the f-$\hat{z}_0$ curve, Fig. 4(d), and this impairs the calculation of deformation and causes deviations from the literature. Furthermore, the negative minimum force that emerges for small deformations corresponds to a maximum attractive force that is also known as the pull-off force. It signifies the force required to move the microbubble away from the cantilever once adhesion has been established. Clearly, this is a very small force for the particular MB that is interrogated in Fig. 4 owing to the very small value of the interaction potential that was introduced for the purposes of comparison against results available from the literature. When actual afm measurements are simulated, the measured pull-off force is a reliable marker that can be used to estimate the interaction potential of the shell and cantilever.

In Fig. 4(b), we plot the shape of the deformed microbubble that corresponds to flat and buckling solutions as obtained with the novel methodology that are almost indistinguishable from the equivalent shapes from the literature. In addition, eigenvalue analysis of the Jacobian matrix was performed as the dimensionless distance $\hat{z}_0$ varied and it was seen that only the stable part of the bifurcation diagram obtained with the classical formulation was recovered in the form of a single unified branch, i.e., the initial Reissner regime followed by the Pogorelov post-buckling regime that emerged when the contact region exceeded the threshold value of, roughly, 10°, also in agreement with the literature. The above picture was completed by calculating the total energy of the two branches and, as it was expected, it acquired the same values with the ones obtained by the standard formulation with the post buckling curve being energetically favorable after the buckling point, Fig. 4(c). It is also interesting to note that the distribution of the disjoining pressure, Fig. 4(e), gradually tends to concentrate at the end of the contact area, thus recovering results available from the literature.[44]

Finally, following the above benchmark calculations against theoretical results in Figs. 5(a) and 5(b), we present a preliminary comparison with afm data available from the literature.[22,30] In particular, simulations with the disjoining pressure model and elastic properties which correspond to MBs covered with polymer as in the work of Elsner *et al.*[22] show satisfactory agreement. The fem curve initially exhibits a linear response with the same slope as the experimental one while around $\Delta = 52$ nm we observe transition to the non-linear regime where buckling takes place, see also the embedded graph. At relatively high deformations, the response in both the fem and experimental curves is slightly curved upwards, which is due to the gas compression. However, the experimental data exhibit instabilities that are manifested in the negative slope of the force deformation curve, which are probably due to defects, 3d, plastic deformations, or even viscoelastic creep effects,[58] which the present model does not account for.

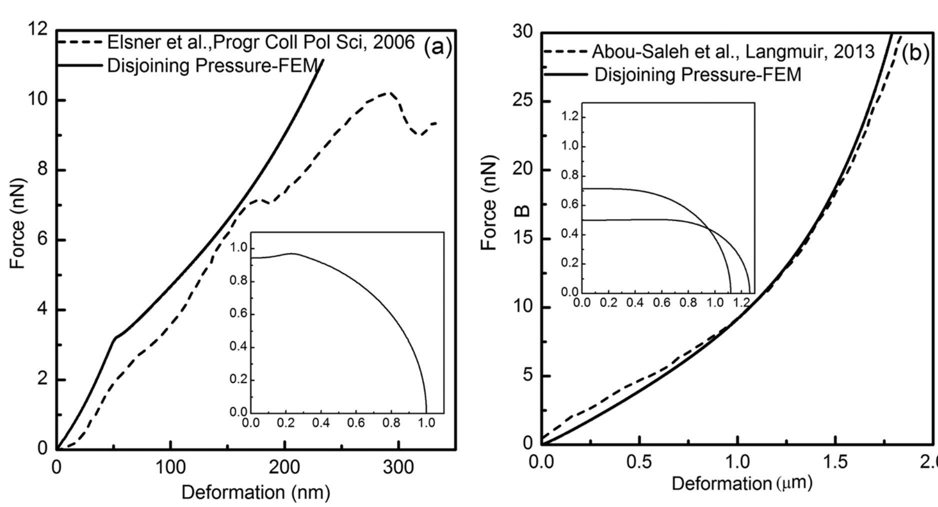

FIG. 5. (a) Comparison between the present numerical model and experimental force-deformation curve by Elsner *et al.*[22] The simulation parameters are E = 252 MPa, h = 25 nm, ν = 0.33, R_0 = 7.9 μm, $W_0 = 10^{-5}$ N/m, and δ_A = 20 nm with Hooke's constitutive law; embedded shape obtained at deformation 150 nm. (b) Comparison between the present numerical model and experimental force-deformation curve by Abou-Saleh *et al.*[30] The simulation parameters are $\chi = 7.7 \times 10^{-3}$ N/m, $k_b = 1.76 \times 10^{-15}$ Nm, ν = 0.5, R_0 = 1.75 μm, $W_0 = 10^{-5}$ N/m, and δ_A = 50 nm with the Mooney-Rivlin constitutive law; embedded shapes obtained at deformations 1 μm and 1.7 μm.

Hence the simulated curve in Fig. 5(a) was not pursued beyond deformations on the order of 200 nm, for which the experimental curve is dominated by such instabilities. Moreover, we compare our model with afm data for MBs covered with phospholipid monolayer that were obtained by Abou-Saleh *et al.*[30] In this case, the simulation parameters are obtained via the experimental curve and employment of the methodology for parameter estimation proposed in Sec. IV. The two curves are in excellent agreement, revealing the validity of the method proposed herein. In particular, both curves initially exhibit a linear response while subsequently instead of buckling, a strong curved upwards regime is obtained which is dominated by gas compressibility. In this case, simulations also show that buckling is bypassed and the shell around the pole area where contact takes place remains flattened, see also the embedded shapes in Fig. 5(b).

IV. ASYMPTOTIC ANALYSIS

The above theoretical formulation can provide an accurate solution of the required force to achieve a certain deformation in the context of axisymmetry. However, a simpler analytical model that relates the force with the deformation will be very useful in order to better interpret the physical mechanisms behind the observed/calculated response patterns and provide the tools for extracting the shell elastic parameters out of f-d curves obtained via afm measurements. The f-d curves obtained from hard shells usually exhibit linear response followed by a non-linear regime curved downwards, Fig. 6(a). Theory and simulations suggest that in the former regime the shell remains flattened, while in the latter buckling takes place. Thus, we have proposed in a previous article[26] the classic relations developed by Reissner[23] and Pogorelov[24] for the asymptotic description of this response. In this section, we will illustrate the manner in which this response pattern emerges in the context of the model proposed herein that calculates a smooth load distribution via an interaction potential. The asymptotic structure that identifies a contact, transition, and outer region on the shell interface with the ultra-thin water film that occupies the space between the shell and the hydrophilic cantilever will be employed that has been previously used in the literature[38,39] in order to describe cell adhesion. In this fashion, it will be possible to reveal the underlying mechanism behind unconventional response patterns, such as those obtained when soft shells are statically interrogated, see Fig. 7(a), in which case the initial linear response is followed by a nonlinear curved upwards regime.

The graphs in Figs. 6 and 7 are obtained numerically for a hard, $\hat{P}_A = 3 \times 10^{-3}$, and a soft shell, $\hat{P}_A = 3$, respectively, and present an indicative evolution of shape, load distribution, and energy decomposition with increasing external force pertaining to the above-mentioned static response patterns. In particular, Figs. 6(b)–6(d) portray the transition from flat to dimpled shapes and the corresponding load distribution in the form of the disjoining pressure exerted on the shell. The latter two graphs, in particular, illustrate the fashion in which the load applied on the shell, as the rigid plate approaches thus intensifying the force, transforms from a point load at the pole, Fig. 6(c), to a point load applied at the edge of the contact region, Fig. 6(d). In the latter graph, an internal layer is established at the edge of the contact region, known as the transition layer, that provides a smooth transition in the load distribution between the contact and bulk regions of the shell. The response to a point load distribution was examined in a previous study[26] where deviations were registered in the calculated deformation from numerical results obtained for a rigid plane, i.e., a flat punch, instead of a point load, especially in the Pogorelov regime of buckled shapes. The present methodology provides a very accurate description of the deformation and load distribution, but also, provided a large enough contact length, L, has been established so that it is much larger than the characteristic length of intermolecular forces, i.e., $\delta_A/L \ll 1$, one that is amenable to analysis that provides the structure of the above static equilibria.

In this context, we separate the generatrix of the shell into three regions (contact, transition, and outer) in order to identify the dominant force balance across these areas, Fig. 8. In particular, we identify a flat contact region whose length-scales in the σ and z directions are $L \sim R_0 \sin\theta_c$ and δ_A, respectively, with θ_c denoting the extent of the contact region; similarly the arc length s along the contact region scales like L as well. In this region, the transverse shear q vanishes and the dominant force balance in the normal direction is formed by the disjoining pressure exerted by the film on the shell and the internal microbubble pressure that is adjusted in order to accommodate volume compression. In the tangential direction, in-plane stresses develop in response to area compression of the shell,

$$\vec{n}: P_G - P_A \approx \frac{\partial W}{\partial n}, \tag{28a}$$

$$\vec{t}_s: \frac{\partial \tau_{ss}}{\partial s} \approx -\frac{1}{\sigma}\frac{\partial \sigma}{\partial s}\left(\tau_{ss} - \tau_{\varphi\varphi}\right). \tag{28b}$$

Compressive strain is mainly generated in the adjacent transition region, where significant bending also takes place, and is enforced on the contact region via the matching condition at their interface. As the contact length increases and the above structure is gradually established, see also Figs. 6(c) and 6(d), the load tends to vanish within the contact region and concentrates at its edge where the adjacent region develops characterized by a narrow local peak in the disjoining pressure, Fig. 6(d). This is the structure that is assumed in standard contact studies where a jump is postulated in the load distribution between the contact and free, or outer, regions.[43,44,57]

In the context of the present methodology, this discontinuity is relaxed within an additional internal layer. This is the transition layer where the dominant balance is formed between the disjoining pressure and the bending stresses that develop as a result of the change in curvature that takes place in this region. The length-scales in the normal, n, and tangential, s, directions of the interface in this region are δ/R_0 and ℓ/R_0, respectively, with $\ell \sim \sqrt{R_0\delta}$ in order to conform with the above dominant balance. As the force increases, the interaction potential in the transition region is not characterized by the maximum value w_0, Fig. 6(c). Rather, it is the energy acquired by the shell locally, w_c, as the film compresses to accommodate repulsive

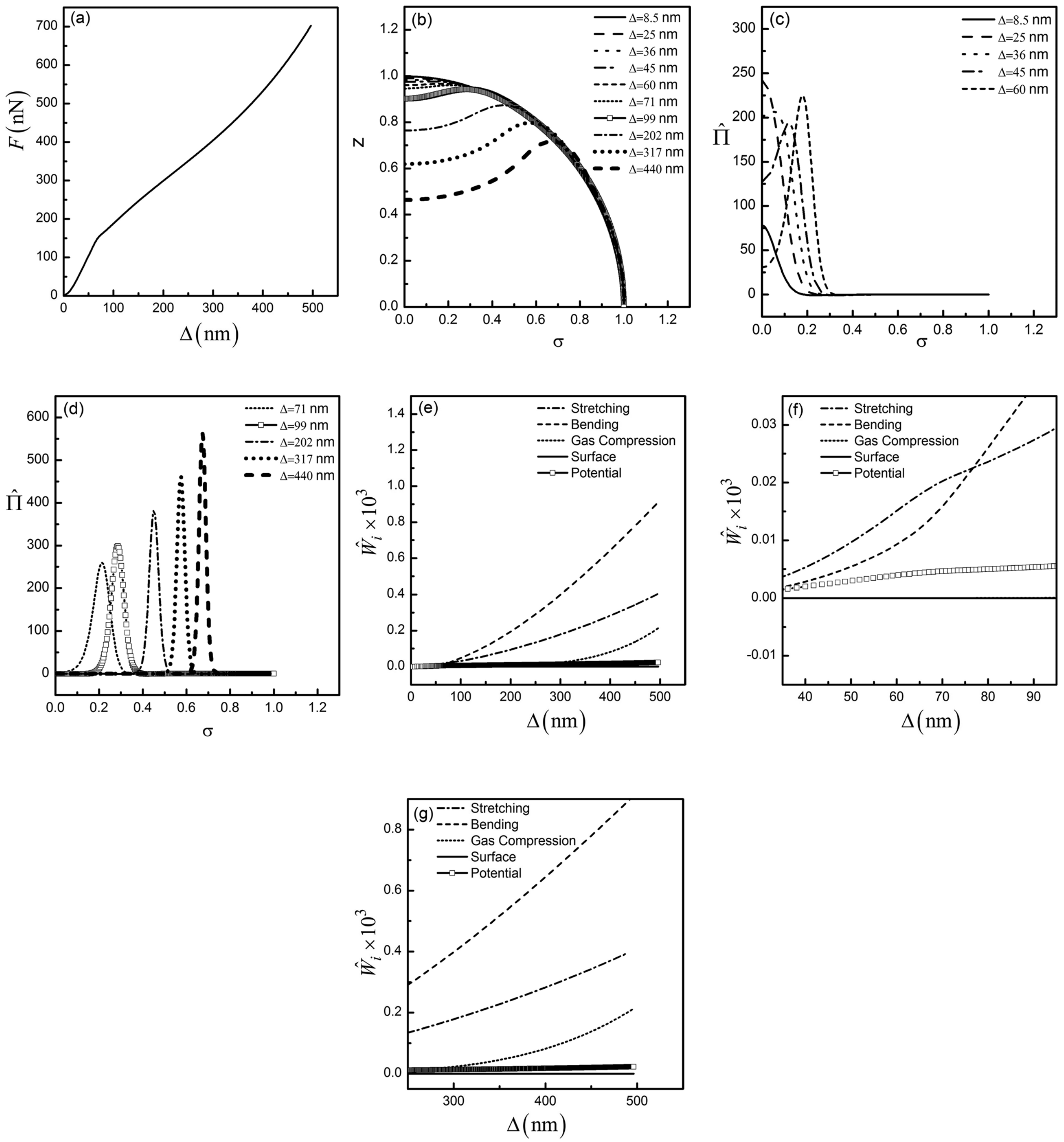

FIG. 6. (a) Force-deformation (F-Δ) curve for a MB covered with polymer type biomaterial, $\left(\hat{k}_b = 3\times10^{-5},\ \hat{P}_A = 3\times10^{-3},\ \hat{W}_0 = 2\times10^{-6},\ \hat{\gamma}_{BW} = 0\right)$, (b) microbubble in the deformed configuration for indicative solutions characterized by flat and buckling shapes. Evolution of the profiles of the dimensionless disjoining pressure $\hat{\Pi}$ as a function of the radial coordinate σ for indicative (c) flat and (d) buckling solutions, (e) components of the dimensionless total energy $\hat{W}_i$ as a function of the deformation, (f) zoom in the energy diagram in the area around the buckling point, (g) zoom in the energy diagram in the area dominated by the gas pressure. Hooke's law is used for the shell with the following physical properties: $R_0 = 1.5\ \mu m$, $E = 2.1$ GPa, $h = 25$ nm, $w_0 = 10^{-4}$ N/m, $\delta_A = 50$ nm, $\gamma_{BW} = 0$ N/m, $\nu = 0.5$.

forces. Consequently, upon introducing

$$n = \frac{n'}{\delta}, \quad \hat{s} = \frac{s' - L}{\ell}, \quad \hat{q} = \frac{q'}{k_b \delta/\ell^3},$$

$$\hat{w} = \frac{w'}{w_c}, \quad L = R_0 \sin\theta, \tag{29}$$

we obtain as the dominant balance in the transition layer

$$\vec{n}:\ \frac{\partial \hat{q}}{\partial \hat{s}} \approx \frac{\partial \hat{w}}{\partial n}\left(\frac{w_c R_0^2}{k_b}\right) \tag{30a}$$

$$\vec{t}_s:\ \frac{\partial \tau_{\hat{s}\hat{s}}}{\partial \hat{s}} \approx -k_s \hat{q}, \tag{30b}$$

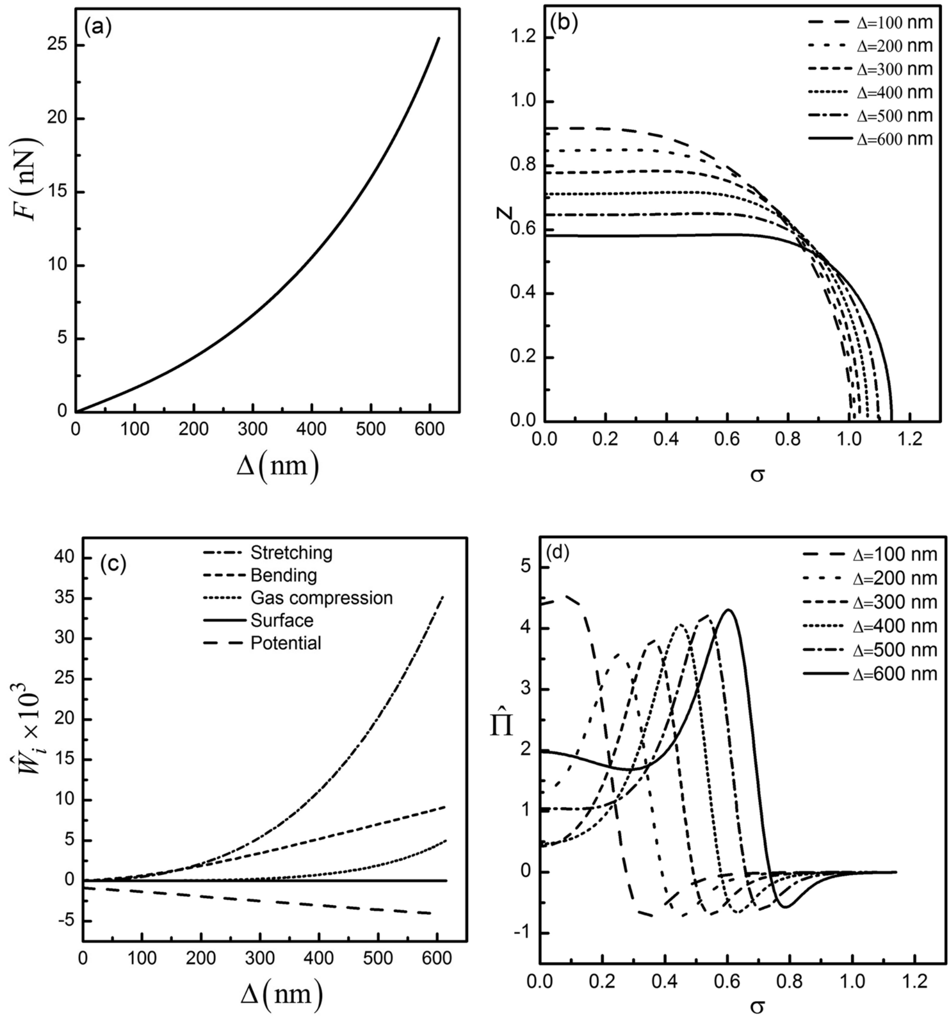

FIG. 7. (a) Force-deformation (F-Δ) curve for a MB covered with lipid type biomaterial $\left(\hat{k}_b = 2.7\times10^{-3}, \hat{P}_A = 3, \hat{W}_0 = 2\times10^{-3}, \hat{\gamma}_{BW} = 0\right)$, (b) deformed shape that corresponds to indicative flat solutions, (c) components of the dimensionless total energy $\hat{W}_i$ as a function of the deformation, and (d) evolution of the profiles of the dimensionless disjoining pressure $\hat{\Pi}$ as a function of the radial coordinate σ. The Mooney-Rivlin law is used for the shell with the following physical parameters: $\delta_A = 50$ nm, $\gamma_{BW} = 0$ N/m, $\nu = 0.5$, $R_0 = 1.5\ \mu$m, $\chi = 0.05$ N/m, $k_b = 3\times10^{-16}$ Nm, $w_0 = 10^{-4}$ N/m.

$$q = \frac{\partial m_{ss}}{\partial s} + \frac{m_{ss}}{\sigma}\frac{\partial\sigma}{\partial s} - \frac{\partial\sigma}{\partial s}\frac{m_{\phi\phi}}{\sigma} \xrightarrow{\hat{m}_{ss}\gg\hat{m}_{\phi\phi}} \hat{q} \approx \frac{\partial\hat{m}_{ss}}{\partial\hat{s}}. \tag{30c}$$

Thus, the transverse shear q that is generated in the transition layer is directly proportional to the repulsive intermolecular forces that develop in that region, $O\left(w_c R_0^2/k_b\right)$, and results in moment, $\hat{m}_{ss}$, exerted on the free part of the shell, as well as the in-plane stress, $\tau_{\hat{s}\hat{s}}$, that compresses the contact region. In fact, the Reissner and Pogorelov regimes are distinguished by the fact that the later in-plane stress on the contact region is finite and zero, respectively, reflecting the state of compression of the flat contact region and the state of fully inverted spherical shell that is established in the same region in the post buckling regime, see also Fig. 6(b). Finally, the total force exerted on the shell within the contact and transition zones is

$$F = F_C + F_{Tr} \approx (P_G - P_A)\pi L^2 + q'2\pi L \sim q'2\pi R_0 \sin\theta_c,$$

$$q' = \hat{q}\left(k_b\frac{\delta_A}{\ell^3}\right) = \frac{w_c R_0}{\sqrt{\delta R_0}}\int \frac{\partial\hat{w}}{\partial n}d\hat{s}, \tag{31}$$

where the component of the force exerted in the transition region is dominant in the Reissner and Pogorelov regimes for which the load nearly vanishes in the contact region, $P_G \sim P_A$. In the above, $k_\varphi \ll k_s$ in the transition region, where $\sigma \sim R_0\sin\theta_c \gg \ell$. The shape of the shell in the transition region is provided by solving the above Eqs. (30) and (31) along with appropriate matching conditions with the contact and outer regions.

Furthermore, as can be surmised by Eq. (30c), the in-plane stress at the edge of the contact region is $\tau_{\hat{s}\hat{s}} \sim \hat{q}$. Based on the standard solution of Eqs. (28) for the contact region[43] where negligible shear stress q is assumed, at the joining point with the transition region, $\tau_{ss} \sim \rho/\theta_c \sim \hat{q}$, with ρ denoting the shell deformation perpendicular to its axis of symmetry. At the same

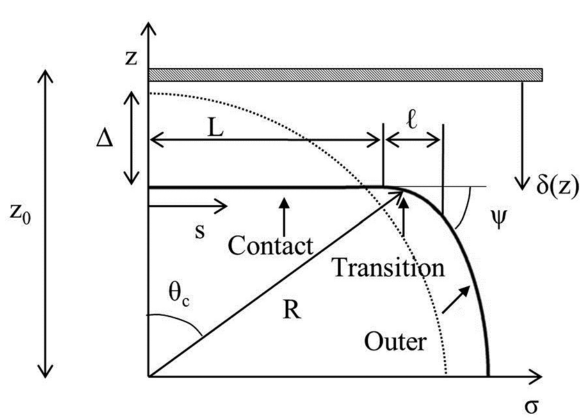

FIG. 8. Schematic representation of the contact, transition, and outer regimes along the shell surface.

time, it can be easily seen that $\rho \sim \theta_c{}^2$ at the edge of the contact region for an initially spherical shell.[43] As a result, $\hat{q} \sim \theta_c \sim w_c R_0^2/k_b$ in order to accommodate the above relations and the total force on the shell scales like $\theta_c{}^2 \sim \Delta z_0/R_0 = \Delta/R_0$, see also Eq. (31), which corroborates the linear response of the f-d curve in the regime of flat contact. Reissner[23] employed the fourth order equations of the theory for shallow spherical shells for rotationally symmetric stretching and bending subject to a uniform load distribution around a small circular area around the pole and obtained the following linear relation:

$$F = \frac{4}{\sqrt{3\left(1-\nu^2\right)}} \frac{Eh^2}{R_o}\Delta \quad \text{or} \quad F = 8\sqrt{\chi k_b}\frac{\Delta}{R_o}. \tag{32}$$

In this limit, the shell is deformed around the pole where it remains flat, whereas it is spherical in the outer part that is free from load, thus identifying the Reissner solution with the above-described linear regime.

Similarly, the structure of the static arrangement with dimpled shapes can be recovered by focusing on the bending and stretching energy that develops within the transition region as the external force further increases and large deformations develop. As the compressive in-plane stresses at the intersection with the contact region increase, a threshold exists beyond which crater formation is a preferred equilibrium state instead of flattened shapes. In this fashion, compressive stresses are relaxed and an inverse spherical shell emerges in the contact region,[57] see also Fig. 6(b). In this case, the disjoining pressure exhibits significant deviation from zero only within the transition layer where it develops an abrupt peak where almost all bending takes place, Figs. 6(b) and 6(d). The formulation in this region is similar to the case with flat shapes with the exception of the requirement for vanishing in-plane stress that has to be substituted in the matching conditions to the region around the pole. In the transition region, the dominant bending and stretching strains are developed along the meridional direction s that also determine the angle θ_c at the point where contact is made with the cantilever, $\theta_c \sim \delta/\ell$. In the same context and using similar geometric scalings, Pogorelov[24] suggested a non-linear analytical expression for larger deformations when buckling takes place,

$$F = \left[\frac{3.56E^2h^5}{\left(1-\nu^2\right)^2 R_o^2}\Delta\right]^{0.5}, \tag{33}$$

based on an energy minimization criterion in the region where bending dominates. Alternatively, resorting to Eq. (31) for the total force while accounting for the fact that $\delta/\ell \sim \theta_c$ and $w_c R_0^2/k_b \approx \theta_c$ also provides an $O(\theta_c)$ dependence of the total force in this regime. Combination of the transition from Reissner to Pogorelov regimes, as described via the above relations (32) and (33), provides reliable estimates of Young's modulus (E) and shell thickness (h) of the shell coating for hard polymeric type MBs, e.g., polymer polylactide,[25,26] that respond in the manner illustrated by Fig. 6(a), based on simulated and experimental f-d curves, without prior knowledge of the thickness.[26] Figure 9(a) provides such a successful parameter estimation on the numerically obtained static response shown in Fig. 6(a).

In the outer problem, lengths scale with the microbubble radius, the disjoining pressure is negligible, and a very similar version of the classic contact problem is recovered,[43,44,57]

$$\vec{n}: P_G - P_A = k_s\tau_{ss} + k_\varphi\tau_{\varphi\varphi} - \frac{1}{\sigma}\frac{\partial(\sigma q)}{\partial s} + 2k_m\gamma_{BW}, \tag{34a}$$

$$\vec{t}_s: \frac{\partial \tau_{ss}}{\partial s} + \frac{1}{\sigma}\frac{\partial \sigma}{\partial s}\left(\tau_{ss} - \tau_{\varphi\varphi}\right) + k_s q = 0, \tag{34b}$$

$$q = \frac{\partial m_{ss}}{\partial s} + \frac{m_{ss}}{\sigma}\frac{\partial \sigma}{\partial s} - \frac{\partial \sigma}{\partial s}\frac{m_{\phi\phi}}{\sigma}, \tag{34c}$$

$$P_G V^\gamma = P_{G0} V_0^\gamma, \tag{34d}$$

coupled with symmetry conditions at the equatorial plane, the kinematic condition on $\hat{z}_0$, and matching conditions at the joining point with the transition region,

$$s = \xi = 0: z = 0, \quad \frac{dz}{ds} = 0, \quad \frac{d\sigma}{ds} = 1,$$
$$m_{ss} = m_{sc}\left[1 + O\left(\frac{w_c R_0^2}{k_b}\right)\right], \quad \xi = 1: z = z_0(F=0) - \Delta z_0,$$
$$\frac{d\sigma}{ds} = 0. \tag{35}$$

Distance $\hat{z}_0$ is a more appropriate geometrical property imposed on the outer problem than the angle of contact θ_c since the latter is not as easy to measure in an experiment. In classic solutions of the contact problem,[43,44,57] angle θ_c is used as a condition along with the dimensionless bending moment $m_{sc} = 1 + \nu$ calculated within the flat contact region.

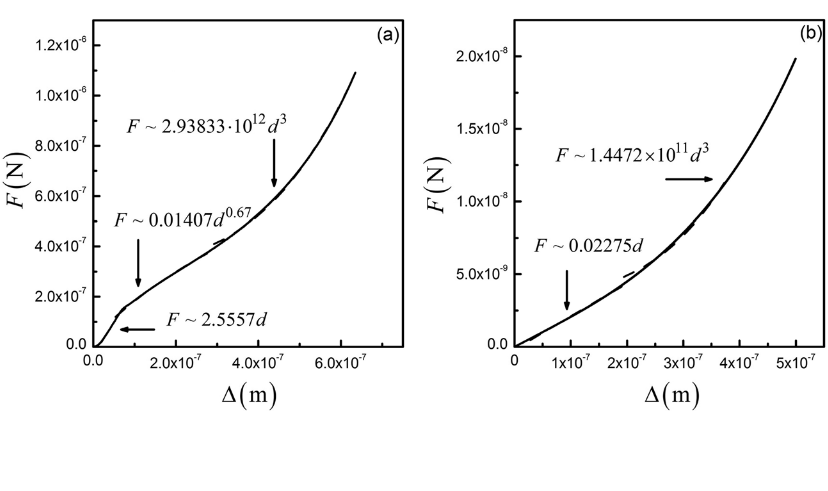

FIG. 9. Numerical F-Δ curves with fitting in the linear (Reissner) regime, non-linear curved downwards (Pogorelov) regime, and the non-linear (curved upwards) regime dominated by gas compression. (a) $\chi = 51$ N/m and $k_b = 3.4 \times 10^{-15}$ N m $\left(\hat{k}_b = 3 \times 10^{-5},\ \hat{P}_A = 3 \times 10^{-3}\right)$ and (b) $\chi = 0.05$ N/m and $k_b = 4.673 \times 10^{-16}$ N m $\left(\hat{k}_b = 4.2 \times 10^{-2},\ \hat{P}_A = 3\right)$.

In view of the above, it can be seen that such solutions constitute an outer problem of the contact configuration that is valid in cases for which the interaction potential is negligible, $w_c R_0^2/k_b \ll 1$. As a result, the bending moments are not significantly modified within the transition layer, the latter is absorbed in the outer region, and the flat contact region is in direct contact with the outer one.

Experimental[29] and numerical f-d curves for microbubbles covered with a soft lipid monolayer exhibit a very different response pattern. Initially the response is linear, but the transition to Pogorelov type response is bypassed by a curved upwards regime dominated by gas compression as indicated by the numerical simulations obtained in the present study, see also Fig. 7(a). Furthermore the shape of the microbubble does not exhibit crater formation as the external load increases. Rather, the MB shape remains flat with a progressively increasing contact region, Fig. 7(b). Consequently, it is expected that using the above-mentioned transition from the Reissner to Pogorelov type response for soft shells will not provide reliable estimates of their elastic properties. However, as indicated by the simulations and illustrated via the distribution of the disjoining pressure, Fig. 7(d), the linear Reissner regime does exist for small deformations for which compressive in-plane stresses in the contact region are not prohibitive energetically. The curved upwards regime is associated with the onset of considerable rise in the internal gas pressure and a concomitant uniform reduction in the film thickness in order to accommodate the balance in the contact region; this is verified by the evolution of the disjoining pressure and energy distribution among the different components, Figs. 7(c) and 7(d). When gas compressibility is of central importance in the response of coated bubbles to external forcing, it is the balance between pressure drop across the interface and in-plane stresses in the main part of the shell that determine the f-d curve.[20,21] Proceeding along the same lines as these earlier studies, in the analysis presented below, we obtain an asymptotic relation for the force exerted on the symmetrically compressed microbubble depicted in Fig. 8, as a function of deformation. Assuming a relatively weak interaction potential, we treat the bubble as almost spherical in this process, at least for not very large loads.

In the absence of an initial pre-stress, the shell is taken to be spherical with pressure P_0 equal with the external pressure, P_A, and volume, $V_0 = 4\pi R_0^3/3$. Assuming that the contact length $L \approx R_0 \sin\theta_c$, Fig. 8, is smaller than the initial MB radius, i.e., θ_c relatively small, but larger than the size of the transition layer, $L \gg \ell$, and that the shell remains shallow, $\Delta \ll z_0 - \Delta z_0$, we obtain the following estimate for the shell volume when it is inflated at the equator, $R = R_0 + \delta R$, due to the external force and at the same time it is flattened at the two poles. In the last two regions, the shell volume is decreased by an amount equal to the volume of two spherical sectors of radius R and angle θ_c, in which case the total volume reads as

$$V = \frac{4\pi R^3}{3}\left[1 - \frac{3}{2}\cos\theta_c + \frac{\cos^3\theta_c}{2}\right] \xrightarrow[\theta_c \text{ small}]{\text{Isothermal Compression}} P_G = \frac{P_A}{1 - 3\theta_c^4\left(\frac{1}{8} - \lambda\right)} \quad \delta R/R_0 \equiv \lambda\theta_c^4. \tag{36}$$

Next, treating the shell as neo-Hookean with negligible bending in the outer region and an almost spherical shape, we obtain the following force balance:

$$P_G - P_A \approx \frac{2\chi}{R}\left(\frac{R^2}{R_0^2} - 1\right) \approx \frac{2\chi}{R_0\left(1 + \lambda\theta^4\right)}\left[\left(1 + \lambda\theta^4\right)^2 - 1\right]$$
$$\approx \lambda\frac{4\chi}{R_0}\theta^4. \tag{37}$$

Upon combining the last two equations, we recover the following relation for λ and the pressure drop across the shell:

$$\lambda = \frac{1}{8}\frac{1}{\left(\frac{4\chi}{3R_0P_0} + 1\right)}, \quad P_G - P_A = 3P_A\theta^4\left(\frac{1}{8} - \lambda\right). \tag{38}$$

In this fashion, the force exerted on the shell at the contact region reads as

$$F_C = (P_G - P_A)\pi L^2 \approx (P_G - P_A)\pi R_0^2 \sin^2\theta \xrightarrow{\theta \text{ small}} F_C \approx 3\theta^6\pi R_0^2 P_0\left(\frac{1}{8} - \lambda\right) \xrightarrow{(38)}$$
$$F_C \approx \theta^6\pi R_0^2 P_0\frac{3}{8}\left(1 - \frac{1}{\frac{4\chi}{3R_0P_0} + 1}\right) \xrightarrow{\chi/(R_0P_0) \ll 1} F_c \approx \pi R_0\chi\frac{\theta_c^6}{2} \xrightarrow{\frac{\Delta}{R_0} \sim \frac{\theta_c^2}{2}} F_c \approx \frac{4\pi\chi}{R_0^2}\Delta^3, \tag{39}$$

$$\chi = \frac{F}{\Delta^3}\frac{R_0^2}{4\pi}. \tag{40}$$

Equation (40) was obtained by Lulevich *et al.*,[20] when the Poisson ratio is set to $\nu = 0.5$ and an incompressible capsule is treated rather than a bubble. Equation (39) is valid for a coated microbubble, $\chi/(P_0R_0) \sim 1$, in the regime for which the dominant part of the load arises as a repulsive force in the contact region due to the thinning of the water film, instead of the transition layer.

Based on the above analysis, it is proposed that Reissner's linear formula, which holds when the force on the shell is balanced by bending stresses in the transition region, can be combined with the above formula, in order to provide reliable estimates of the shell area dilatation modulus and bending stiffness without employing the concept of a shell thickness. Figure 9(b) provides a comparison between numerical simulations of the f-d curve and the combination of formulas (32) and (39) calculated with the same area dilatation and bending modulus, $\chi = 0.015$ N/m, $k_b = 1.558 \times 10^{-15}$ Nm, pertaining to a soft MB with $R_0 = 1.5$ μm, $w_0 = 10^{-4}$ N/m, $\delta_A = 12.5$ nm, $\gamma = 1.07$, and $\gamma_{BW} = 0$. Alternatively, fitting formulas (32) and (39) on the simulated f-d curve provides very similar values for the area dilatation and bending modulus with those used in the simulation. It is anticipated that this procedure can also be successfully applied on experimental f-d curves obtained for polymeric and phospholipid shells, but this investigation is left for a future study.

V. RESULTS AND DISCUSSION

In this section, we present an extensive parametric study on the response of coated microbubbles covering a wide range of the dimensionless parameters, primarily the dimensionless bending resistance and resistance to gas compression, $\hat{k}_b$, $\hat{P}_A$, but also the dimensionless intermolecular and surface tension forces, $\hat{W}_0$, $\hat{\gamma}_{BW}$. We eventually intend to simulate afm experiments involving microbubbles covered with polymeric and phospholipid shells, which are biomaterials very often used in medical applications and respond very differently under the compression from a flat surface due to their different elastic properties. Based on preliminary analysis[26] of afm measurements[25,29] of both types of shells, polymeric shells are characterized by a much larger area dilatation modulus than lipid shells, e.g., $\chi = Eh \approx$ 5-150 N/m, and bending stiffness k_b varying between 10^{-15} and 10^{-18} Nm for a stress free radius R_0 on the order 2 μm's, whereas lipid shells are softer, e.g., $\chi = Eh \approx$ 0.01-0.1 N/m. A typical set of physical parameter values for a polymeric shell is provided in the literature for microbubbles coated with a polylactide shell[25,26] that follows a neo-Hookean constitutive law; $R_0 = 1.5$ μm, $E = 2.1$ GPa, $h = 25$ nm, $\nu = 0.5$, $\gamma_{BW} = 0$ N/m, $\gamma = 1.07$, $w_0 = 10^{-4}$ N/m, and $\delta_A = 50$ nm, setting the dimensionless parameters to $\hat{k}_b = 3 \times 10^{-5}$, $\hat{P}_A = 3 \times 10^{-3}$, $\hat{\gamma}_{BW} = 0$, $\hat{W}_0 = 2 \times 10^{-6}$, and $\hat{\chi} = 1$. For the case of a lipid shell, indicative physical parameter values are provided in the literature[29] for a phospholipid monolayer shell obeying the Mooney-Rivlin constitutive law with b = 1; $R_0 = 1.5$ μm, $\chi = 0.05$ N/m, $k_b = 3 \times 10^{-16}$ Nm, $\nu = 0.5$, $\gamma_{BW} = 0$ N/m, $\gamma = 1.07$, $w_0 = 10^{-4}$ N/m, and $\delta_A = 50$ nm, thus setting the dimensionless parameter values to $\hat{k}_b = 2.7 \times 10^{-3}$, $\hat{P}_A = 3$, $\hat{\gamma}_{BW} = 0$, $\hat{W}_0 = 2 \times 10^{-3}$. To accommodate such a wide variation of physical constants, the area dilatation modulus primarily, we employ $\hat{P}_A$ values ranging between 10^{-4} and 3 as a means to distinguish between the response patterns that characterize polymeric and lipid shells, respectively, for micron size MBs in an atmospheric pressure environment. Similarly the effect of dimensionless bending stiffness, $\hat{k}_b$, is investigated in the range between 2×10^{-6} and 2×10^{-2}, whereas $\hat{W}_0$ and $\hat{\gamma}_{BW}$ are initially set to 2×10^{-6} and 0, respectively, and allowed to increase from these values onwards.

A. Parametric study for hard shells, $\hat{P}_A \ll 1$

We perform an extensive parametric study, employing our novel methodology that introduces intermolecular forces as a means to obtain the load distribution, varying the relative resistance between gas compression and strain, $\hat{P}_A = (P_A R_0)/\chi$. Very small values of $\hat{P}_A \ll 1$ are tested denoting hard shells with large area dilatation modulus $\chi \gg 1$. Once parameter $\hat{P}_A$ is fixed, parameter $\hat{k}_b = k_b/\left(\chi R_0^2\right)$ is varied thus fixing the shell bending resistance, k_b. A weak interaction force with the cantilever is prescribed as a starting point of the parametric study, $\hat{W}_0 = w_0/\chi = 2 \times 10^{-6}$, with negligible interfacial tension, $\hat{\gamma}_{BW} = 0$.

In this fashion, setting $\hat{P}_A$ to 3×10^{-3} and 3×10^{-4} while employing Hooke's law for the shell, a rich response pattern is revealed as we gradually increase the bending resistance, $\hat{k}_b$, reflecting the interplay between the three major stiffnesses, i.e., resistance to straining, bending, and gas compression; the resistance to compression of the ultrathin film between the shell and cantilever is negligible. As can be gleaned from Figs. 10(a) and 10(b), for such hard shells, the f-d curve exhibits the standard pattern of linear, Reissner, response followed by the nonlinear, Pogorelov, regime, indicating the buckling transition as a means to relax excessive compressive straining. As a result, the force required to achieve a certain deformation increases in a milder fashion than in the linear regime. This response pattern in the f-d curve is reflected in the transition from flat to dimpled shells in the region around the pole, see also Fig. 6(b). One more interesting aspect of this simulation is the distribution of the disjoining pressure, Figs. 6(c) and 6(d). In the linear regime of flattened shapes around the pole region, the load is essentially applied at the end of the contact area as we have already seen in the benchmark calculations, Fig. 6(c). When buckling takes place, the pressure is essentially applied around a ring in the dimple region of the deformed shape, Fig. 6(d). Eventually, as the distance between the shell and cantilever is further decreased, the exerted force increases significantly and the f-d curve curves upwards indicating the fact that the resistance to volume compression dominates the response. In the linear and curved downwards regime, volume reduction is negligible, but at high deformations, the shell shrinks significantly and consequently the internal pressure becomes an important additional stiffness in the equilibrium increasing the required force for deformation. The above three regimes detected in the f-d curve can also be represented by the relative importance of the individual energy components, Figs. 6(e)–6(g). In the linear regime, the main balance is between the elastic energies (stretching ~ bending), with stretching representing the dominant component, Fig. 6(f). After the buckling point, it is elastic effects that control the total response, but we observe an exchange in the relative importance in favor of bending, Fig. 6(f). This happens because in the buckling stage we have an almost reversed spherical cup in the contact area that significantly reduces the extent of

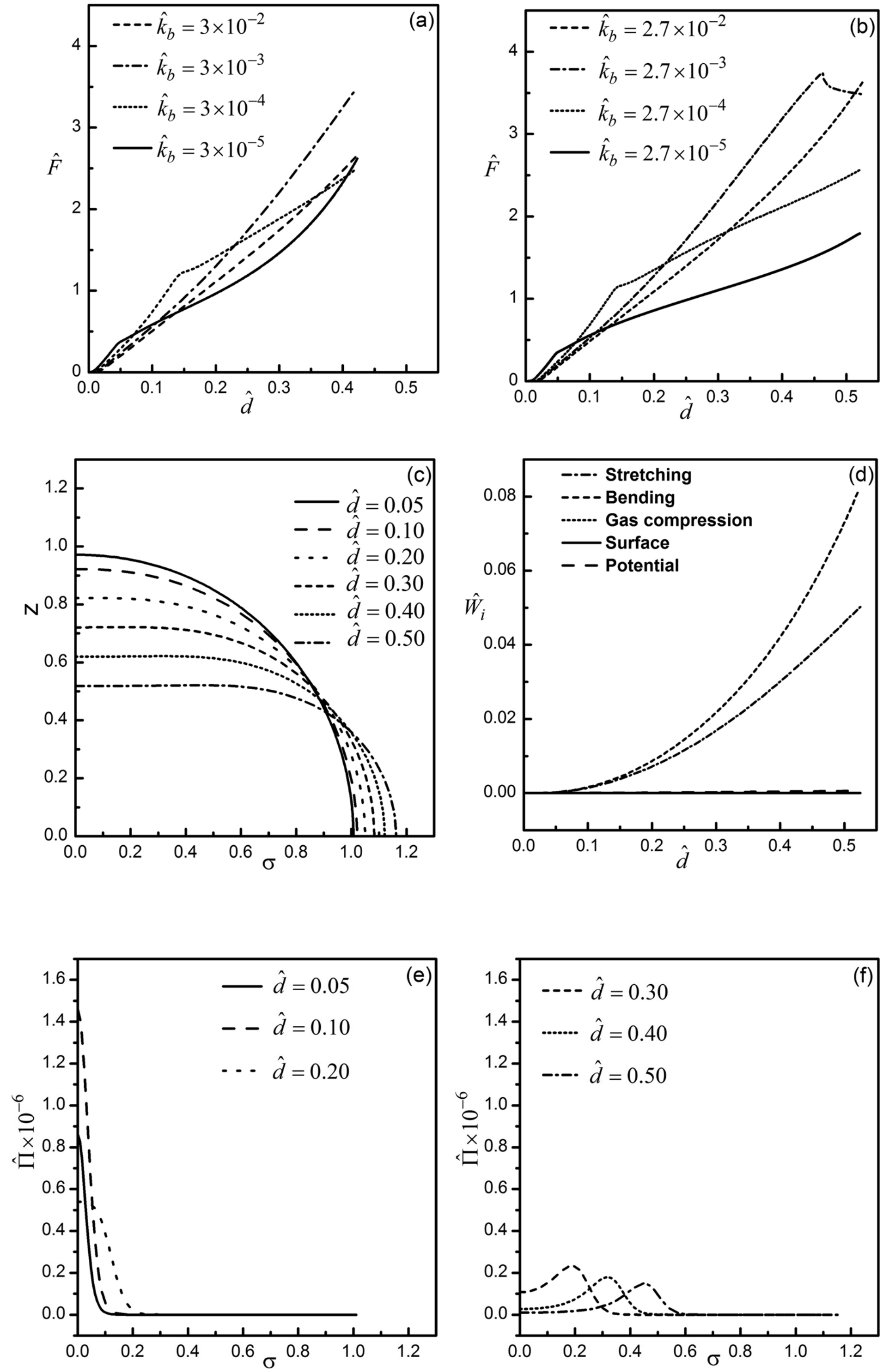

FIG. 10. Parametric study for the effect of dimensionless bending modulus $\hat{k}_b$ in dimensionless force-deformation curves when (a) $\hat{P}_A = 3 \times 10^{-3}$ and (b) $\hat{P}_A = 3 \times 10^{-4}$. Evolution of (c) shapes, (d) dimensionless energy components $\hat{W}_i$ as a function of dimensionless deformation $\hat{d}$, and [(e) and (f)] dimensionless disjoining pressure profiles $\hat{\Pi}$ along the radial coordinate σ, when $\hat{P}_A = 3 \times 10^{-4}$ and $\hat{k}_b = 2.7 \times 10^{-2}$.

compression while increasing the bending strains. Finally, at large deformations, the energy due to gas compression starts to increase becoming of the same order as the elastic energies, Fig. 6(g). This is directly reflected in the f-d curve with the curved upwards response in the same regime of large deformations.

It should be noted that in the f-d curves of Figs. 10(a) and 10(b) the external force is scaled against $(\chi k_b)^{1/2}$ in order to clearly illustrate the extent of validity of the Reissner regime. Based on classical mechanics,[23] the dimensionless force $\hat{F} = F/(\chi k_b)^{1/2}$ has a fixed slope 8, with Poisson ratio ν set to 0.5, when plotted against relative deformation $\hat{d} = \Delta/R_0$, see also Eq. (32).

Furthermore, the linear regime is valid until relative deformation, $\hat{d}$, is on the order of 2.5 h/R_0, a result that can be easily verified when the resistance to gas compression is negligible, $\hat{P}_A \ll 1$, upon inspection of Figs. 10(a) and 10(b). In addition, as we gradually increase the dimensionless bending modulus, i.e., $\hat{k}_b = 3 \times 10^{-4}$, 3×10^{-3}, and 3×10^{-2}, corresponding to a progressively thicker shell, while keeping the rest of the numbers the same as in Fig. 6(a), the validity of the Reissner regime is extended and the buckling point is shifted toward higher values of the dimensionless force and deformation. In particular, a shell with higher bending modulus, $\hat{k}_b = 3 \times 10^{-4}$, only exhibits the transition from the Reissner to Pogorelov regime and the internal pressure does not affect the response as much since the shell is able to store more bending energy that controls the buckling (Pogorelov) regime. Further increase in the shell thickness, $\hat{k}_b = 3 \times 10^{-3}$, eliminates the post-buckling regime, and the shell exhibits a linear response for the entire range of practically attainable deformations. This reflects the fact that bending becomes very energy consuming in this case, and consequently, in order for the shell to minimize its total energy, it remains in the linear regime where stretching is energetically favorable.

When the area dilatation modulus increases, $\hat{P}_A = 3 \times 10^{-4}$, buckling occurs for a smaller external force for the same shell thickness. However, the range of validity of the Reissner regime still conforms with the 2.5 $h/R_0 \approx 7.5(k_b/\chi/R_0^2)^{1/2}$ rule when $\nu = 0.5$. Consequently, in the rescaled variables used in Figs. 10(a) and 10(b), the location of the buckling point remains the same for the same relative bending stiffness $\hat{k}_b$, as can be gleaned from the above panels. Eventually the f-d curve exhibits the curved upwards regime of dominant gas compression that is now observed at much larger deformations in comparison with Fig. 10(a) and the same $\hat{k}_b$ value. This is a result of the decreased relative resistance to gas compression and the resulting requirement of a larger compression in order to produce a significant effect in the energy balance. The shape for $\hat{k}_b = 2.7 \times 10^{-2}$ and $\hat{P}_A = 3 \times 10^{-4}$ remains flattened for all the range of deformations as the bending stiffness is dominant, Figs. 10(c) and 10(d). The slightly curved upwards response of this f-d curve is accompanied with deviation from sphericity at relatively high deformations in the outer part of the shell, as the length of the contact region approaches the microbubble radius. The above pattern is corroborated by the plot of the disjoining pressure, in which the linear regime exhibits a distribution that is concentrated at the pole region, whereas in the curved upwards part the loading is extended over a larger portion of the contact region, Figs. 10(e) and 10(f).

The parameter that controls adhesion between the MB and the cantilever was set to a quite low value, ($w_0 = 10^{-4}$ N/m), indicating that the interaction is weak, based on preliminary simulations against available f-d curves from afm measurements. In general, however, the case of strong adhesion is also possible depending on the shell material. In this case, the point of zeroforce does not necessarily correspond to an almost spherical undeformed shape. The simulation via the intermolecular forces captures the stable response pattern whether that involves buckling or just a prolonged Reissner type response, and this constitutes a powerful tool for simulating contact problems for a wide range of configurations. In particular, by increasing the adhesion parameter, i.e., setting w_0 to 10^{-1} N/m which gives $\hat{W}_0 = 2 \times 10^{-3}$, and keeping the rest of parameters the same as in Fig. 10(a), buckling is postponed to higher values of force and deformation, Fig. 11(a), or even buckling is bypassed, Fig. 11(b). This is because the adhesive force stabilizes the shell in contact with the cantilever and relaxes the compressive elastic tensions responsible for buckling. In the case of panel (11b), the shell thickness renders buckling energetically unfavorable. Consequently, maintaining a nearly flat contact region provides the energy reduction required for energy minimization of the shell.

The above aspects of the equilibrium subject to strong adhesion are portrayed in Figs. 12 and 13, showing the predominance of flat shapes over a longer deformation range before buckling takes place in Fig. 12(a) and the elimination of buckling for the thicker shell studied in Fig. 13(a). In both cases, energy reduction as a result of strong interaction with the cantilever postpones or even removes buckling as a means of energy redistribution, Figs. 12(b), 12(c), and 13(b). In particular, the evolution of the disjoining pressure with increasing relative deformation, registered for relatively thick shells with $\hat{k}_b = 3 \times 10^{-4}$, extends the range of typical linear response with the load concentrated at the edge of the flat contact region where a gradual thinning of the intermediate water film is captured, Fig. 13(c). Deviations from sphericity and the onset of bending in the outer shell region in both the above cases produce a different slope in the linear part of the f-d curves.

It should also be noted that when the thinner shell is interrogated the solution follows the linear-flat regime beyond

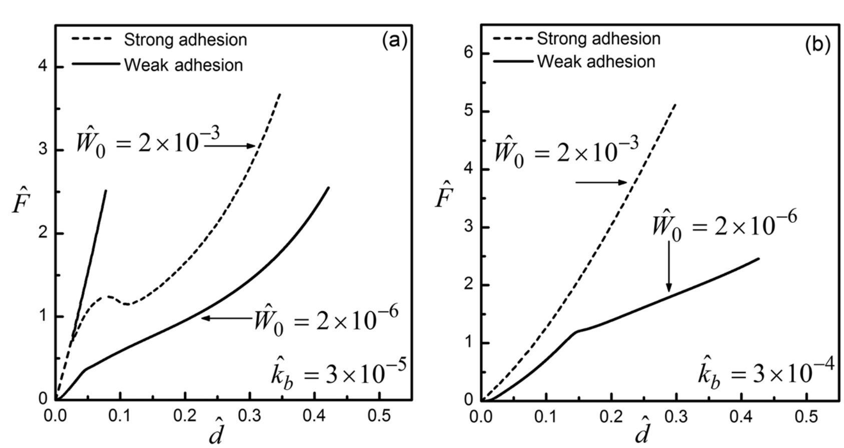

FIG. 11. Effect of the characteristic adhesive energy (w_0) on the dimensionless f-d curve when (a) $\hat{k}_b = 3 \times 10^{-5}$, $\hat{P}_A = 3 \times 10^{-3}$ and (b) $\hat{k}_b = 3 \times 10^{-4}$, $\hat{P}_A = 3 \times 10^{-3}$.

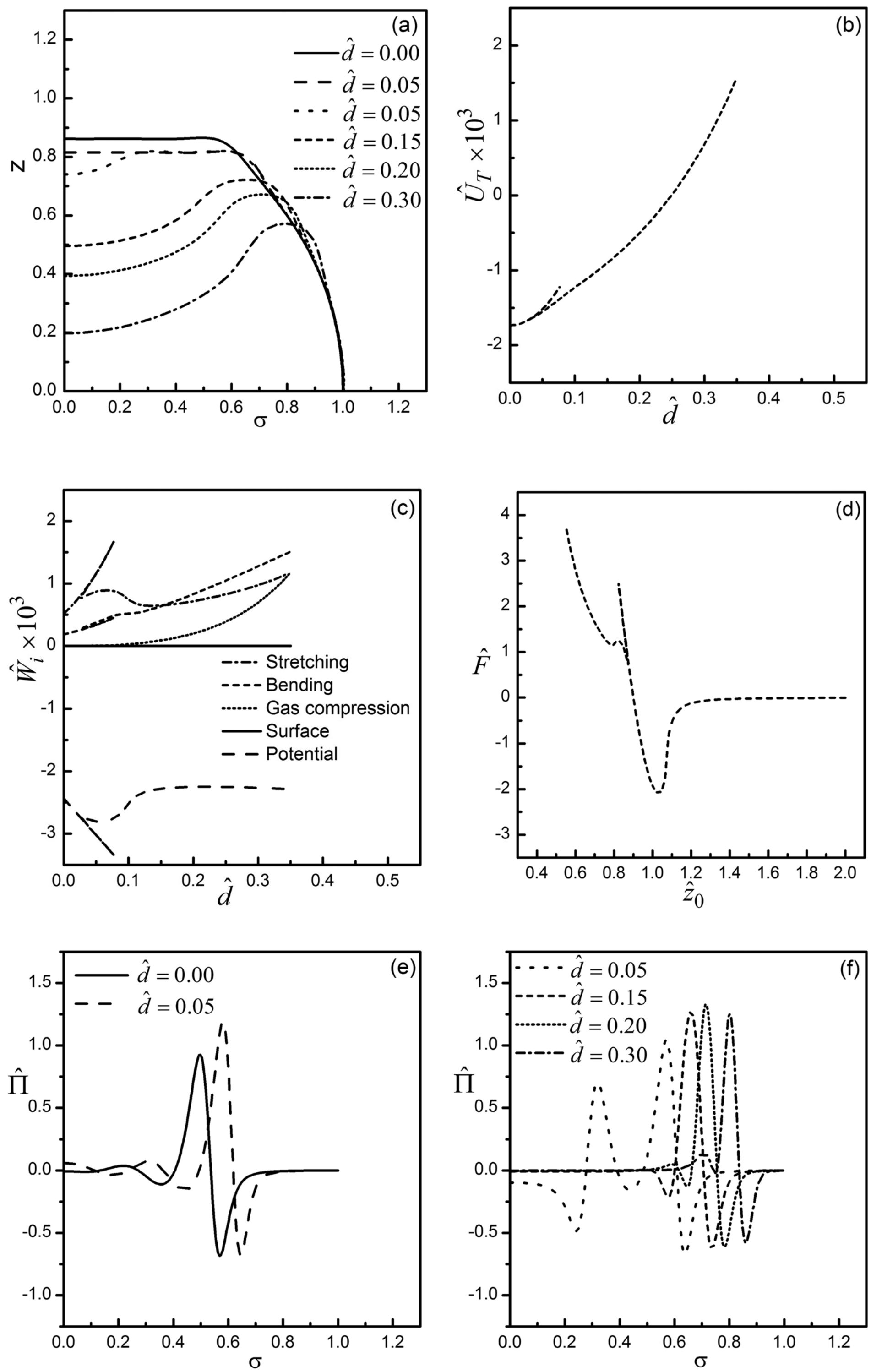

FIG. 12. Evolution of the (a) shapes for indicative solutions, (b) dimensionless total energy $\hat{U}_T$ as a function of dimensionless deformation $\hat{d}$, (c) energy distribution among the different components $\hat{W}_i$ as a function of deformation $\hat{d}$, (d) dimensionless $\hat{F}$ as a function of dimensionless distance $\hat{z}_0$, and [(e) and (f)] evolution of dimensionless disjoining pressure profiles $\hat{\Pi}$ as a function of deformation. The simulation parameters are $\hat{k}_b = 3 \times 10^{-5}$, $\hat{P}_A = 3 \times 10^{-3}$, $\hat{W}_0 = 2 \times 10^{-3}$. The solutions with the same relative deformation $\left(\hat{d} = 0.05\right)$ correspond to points of the pre- and post-buckling branches of Fig. 11 for the strong adhesion case.

the critical deformation for which buckling occurs until after a limit point, at $\hat{d} = 0.07$ and $\hat{F} = 2.5$, it turns down to lower deformations until at $\hat{d} = 0.03$ and $\hat{F} = 0.71$ it exhibits the buckling instability. From the buckling threshold onwards, it follows the classic buckling regime as predicted by earlier studies where multiplicity of solutions was also observed.[43,57] The multiplicity observed in Fig. 11(a) reflects the loss of stability of the linear branch, as it is characterized by higher total energy after the buckling point, see also Fig. 12(b). Eventually, the post-buckling branch is also expected to become unstable as it exhibits a negative slope in the f-d curve.

Finally, the increase in adhesion parameter affects the maximum attraction or pull-off force from the cantilever, which now occurs after a more complex pattern in the translation of the cantilever with respect to the shell, see also Figs. 12(d) and 13(d), and corresponds to a deformed shape depending on the strength of the interaction. This is a common aspect of hard and soft shells and will be demonstrated in more detail in Sec. V B.

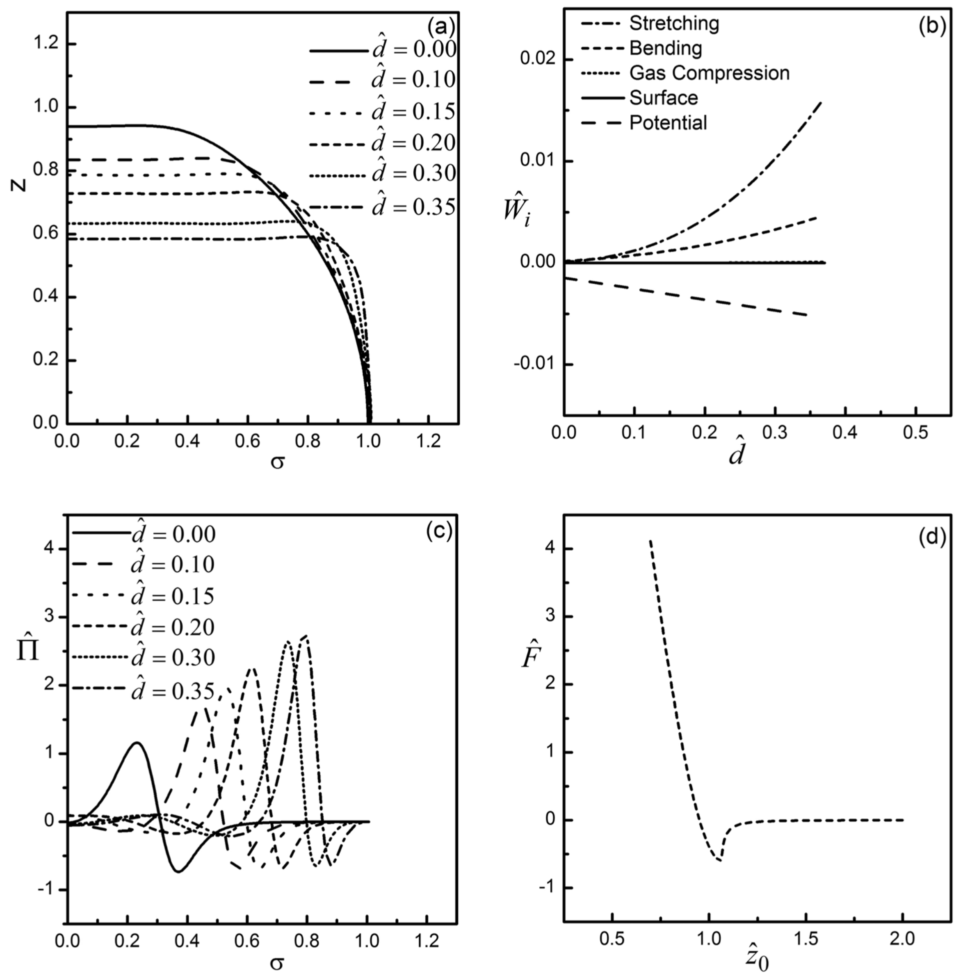

FIG. 13. Evolution of the (a) shapes, (b) dimensionless energy components $\hat{W}_i$ as a function of dimensionless deformation $\hat{d}$, (c) dimensionless disjoining pressure profiles $\hat{\Pi}$ as a function of the radial coordinate σ for indicative solutions, and (d) dimensionless force $\hat{F}$ as a function of dimensionless distance $\hat{z}_0$. The simulation parameters are $\hat{k}_b = 3 \times 10^{-4}$, $\hat{P}_A = 3 \times 10^{-3}$, $\hat{W}_0 = 2 \times 10^{-3}$.

B. Parametric study for soft shells, $\hat{P}_A \sim 1$

In order to examine the static response of soft shells, we set $\hat{P}_A = 3$ indicating a small area dilatation modulus and $\hat{W}_0 = 2 \times 10^{-3}$ for a weak shell-cantilever interaction while gradually increasing the bending stiffness via $\hat{k}_b$. The simulated f-d curve obtained in this fashion differs significantly in comparison with MBs covered with hard shells. More specifically, the response initially follows a linear path, but the transition to a non-linear curved downwards regime of buckled shapes is bypassed directly to the gas dominated regime, see also Fig. 7(a). The shape of the microbubble remains flat without buckling taking place in the contact region, Fig. 7(b). As a result, there was no exchange of energies due to stretching and bending and the Reissner dimensionless slope of nearly 8 was recovered throughout the linear regime. Rather, stretching energy remains the dominant energy component of the equilibrium, Fig. 7(c), for the entire range of relative deformations examined. Moreover, it can be easily noted that the rise of the energy due to gas compression is reflected on the transition from the linear to the non-linear curved upwards response in the f-d curve for $\Delta/R_0 \geq 0.2$ as a manifestation of the dominant balance between external overpressure and compressive strain in the main part of the shell that remains nearly spherical in this non-linear regime. The disjoining pressure profiles also follow a different response pattern in comparison with hard shells. In the linear regime, they exhibit a flat distribution of low values with a positive peak at the edge of the contact region where the distance from the cantilever decreases resembling a point load that is gradually being displaced from the pole, Fig. 7(d). The outer part of the shell that is at a relatively high distance has zero loading, and therefore, no interaction with the cantilever exists there. As the external force increases, the interaction force initially decreases in the pole region as the contact region extends further out. However, instead of reaching zero, indicating the commencement of buckling around the pole region, it starts increasing thus designating a progressive thinning of the film that results in additional repulsion, Fig. 7(d). In order to maintain the normal force balance in the contact region, the shell is compressed and its internal pressure increases signifying the onset of the nonlinear regime in the f-d curve. This transition takes place at, roughly, relative deformation $\Delta/R_0 \approx 0.2$ for which the component of the interaction force that pertains to the contact region becomes dominant, Eq. (31), leading to the nonlinear force deformation curve described in Eq. (39). Figures 14(a) and 14(b) illustrate the effect of increasing bending resistance on the above pattern setting $\hat{k}_b = 2.7\times10^{-5}$, 2.7×10^{-4}, 2.7×10^{-3}, and 2.7×10^{-2}, with $\hat{P}_A$ set to 0.3 and 3, respectively, while the rest of the parameters remain the same as in Fig. 7. As can be gleaned from the above figures, even for the smallest value of $\hat{k}_b$, the f-d curve maintains the transition from the Reissner regime

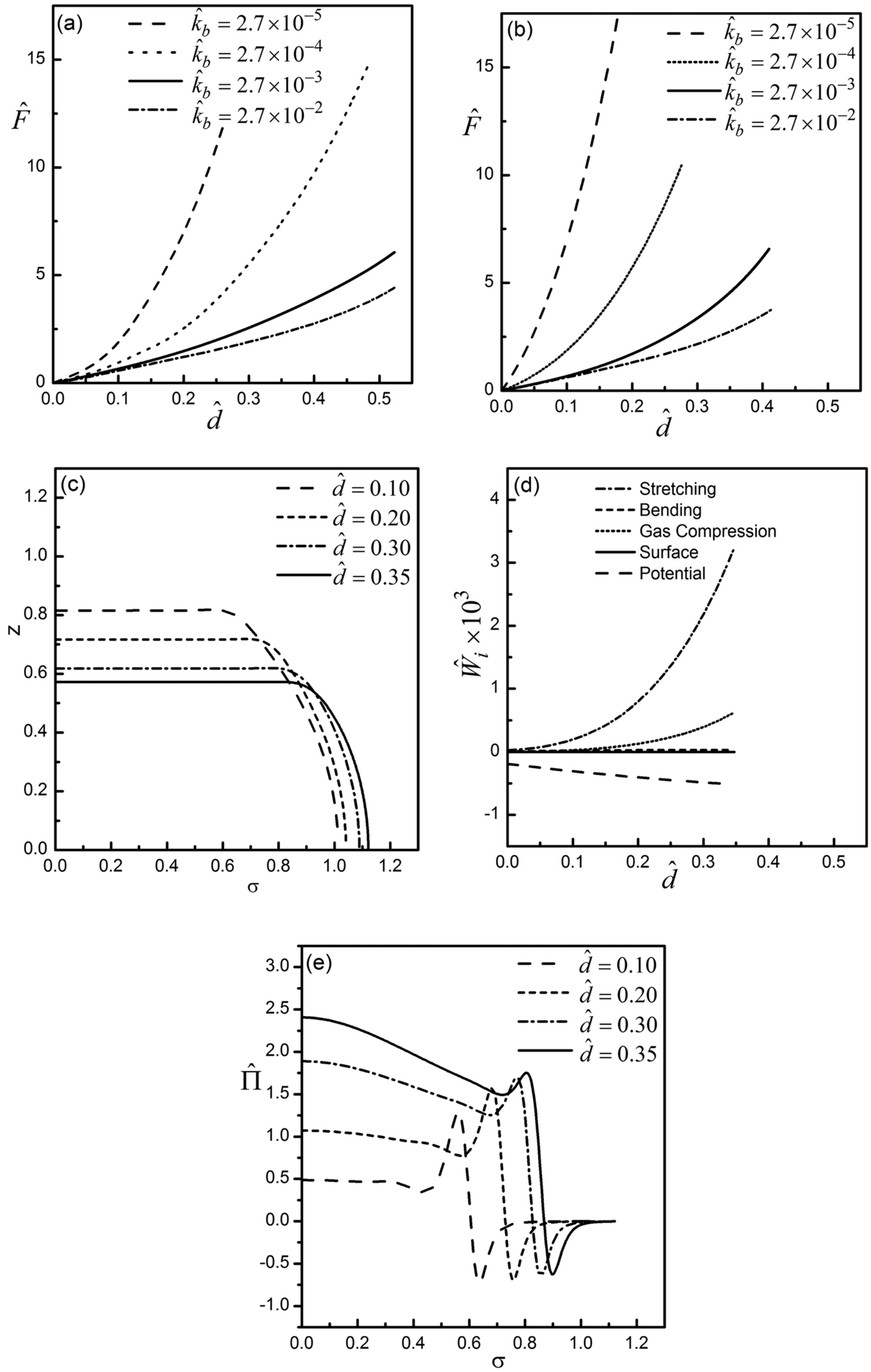

FIG. 14. Effect of dimensionless bending modulus $\hat{k}_b$ in dimensionless force-deformation curves when (a) $\hat{P}_A = 0.3$ and (b) $\hat{P}_A = 3$. Evolution of (c) shapes, (d) dimensionless energy components $\hat{W}_i$ as a function of dimensionless deformation $\hat{d}$, and (e) dimensionless disjoining pressure profiles along the radial coordinate σ for indicative solutions, when $\hat{P}_A = 3$, $\hat{k}_b = 2.7 \times 10^{-5}$, and $\hat{W}_0 = 2 \times 10^{-3}$.

to a gas dominated regime, indicating that when the internal pressure is comparable to elasticity $\left(\hat{P}_A \sim 1\right)$ a new pattern is defined, which changes the classic response, shown in Figs. 6 and 10. Hence, in contrast with similar shells which have the same dimensionless bending modulus, here gas compressibility acts as an extra rigidity that bypasses buckling. In addition, as the bending modulus increases, the validity of the linear (or Reissner) regime is extended toward larger deformations maintaining the standard dimensionless slope of 8 when $\nu = 0.5$. On the contrary for a shell characterized with lower bending resistance, the onset of non-linearity due to gas compression becomes dominant earlier since bending strain is no longer a sufficient source of energy. It should also be stressed that for shells with very low bending stiffness, e.g., $\hat{k}_b = 2.7\times10^{-5}$, and area dilatation modulus, e.g., $\hat{P}_A = 3$, both nonlinearity and deviation from sphericity arrive for very low deformations, see also Figs. 14(a) and 14(b), and as a result, quite elongated compressed shells are obtained that do not exhibit a well-defined Reissner regime nor do they follow the cubic nonlinear response of Eq. (39). Figure 14(c) illustrates the shell shape in the above parameter range indicating flat shapes that exhibit repulsion in the contact region due to progressive thinning of the intervening film. Adhesion constitutes a significant resistance to the cantilever translation, and this reflects in the energy distribution shown in Fig. 14(d), where now stretching dominates over gas compression and bending, leading to an almost linear response albeit with a different slope due to extensive elongation. Furthermore, the disjoining pressure early on develops a strong plateau in the contact region, Fig. 14(e), signifying the onset of significant gas compression. However, this is a rather marginal behavior, and for a wide parameter range, see also Figs. 14(a) and 14(b), the pattern of the linear Reissner response followed by the cubic curved upwards response accurately describes the simulated f-d curves. The onset of nonlinearity depends on the relative importance of resistances to bending and gas compression, but eventually the cubic response is recovered.

As was illustrated by the simulations conducted on MBs coated by a hard shell, a strongly adhered MB requires higher force for deformation while buckling is either postponed or bypassed, see also Figs. 11–13. In the case of soft shells presented in this subsection, buckling phenomena were not captured; nevertheless, increasing the interaction potential, $\hat{W}_0$, increases the required force for a certain deformation to be achieved as well. Figure 15(a) demonstrates how the f-d curve changes for increasing value of the adhesive energy per unit area, w_0. The lowest value of $w_0 = 10^{-5}$ N/m, corresponding to $\hat{W}_0 = w_0/\chi = 10^{-5}/0.05 = 2\times10^{-4}$, does not significantly differ from the 10^{-4} N/m case, and the resulting adhesive force at maximal attraction is almost zero, see also the embedded diagram in Fig. 15(a). On the other hand, when $w_0 = 10^{-3}$ N/m, i.e., $\hat{W}_0 = 2\times10^{-2}$, not only is the repulsive force higher, but also the magnitude of maximum attraction increases significantly. In Fig. 15(b), the f-d curves pertaining to the case of strong adhesion, $\hat{W}_0 = 2\times10^{-2}$ and $\hat{W}_0 = 5\times10^{-2}$, are compared against the f-d curve obtained for weak adhesion when $\hat{W}_0 = 2\times10^{-3}$. The trend is again the same, and the maximum attractive force is now much larger. Both effects are due to the stronger interaction between the shell and cantilever that generates significantly larger forces for the same distance between the cantilever and shell center of mass. In addition, the increase of w_0 leads to f-d curves where the relative position of the cantilever and shell is not a monotonically decreasing function. Thus, arc-length continuation is the most appropriate way to proceed with the numerical evaluation of f-d diagrams, in the regime for which attractive forces prevail between the shell and cantilever.

In this fashion, continuation to small cantilever-shell separations occurs through the onset of two limit points that generate a hysteresis loop. It corresponds to the pull-off force required to equilibrate the strong adhesive force exerted on the shell by the cantilever. As w_0 increases, the attraction is stronger; hence, the shape that corresponds to the onset of repulsion is gradually more deformed in the pole area, as can be gleaned from panels (16a) and (17a) showing the evolution of shape with increasing external force for progressively larger adhesion. During attraction and repulsion, the shape of microbubbles for w_0 in the interval between $\hat{W}_0 = 2\times10^{-2}$ and 5×10^{-2} is characterized by obtuse wetting angles. However, in the case of strongest adhesion, the wetting angle is close to 90°; the values of relative deformation in Figs. 16 and 17 corresponding to each of the deformed shapes shown refer to the equivalent point in the f-d curve. As w_0 increases, the calculated deformations differ significantly in the sense that they are based on the location of the pole in the reference configuration that registers a zero force. When the adhesion is strong, a zero force does not correspond to a spherical shape. On the contrary, the position of the pole is significantly deformed; hence, the resulting deformation differs from the actual pole displacement. During afm experiments, adhesion is typically small. As a result, the measured deformation is very close to the pole displacement from its position corresponding to the spherical configuration. Consequently the model proposed in the present study that incorporates the interaction potential constitutes a promising alternative for obtaining the load distribution and simulating the static response of shells during contact experiments. In particular, identifying the maximal attraction during an afm experiment, or equivalently the pull-off force required to separate

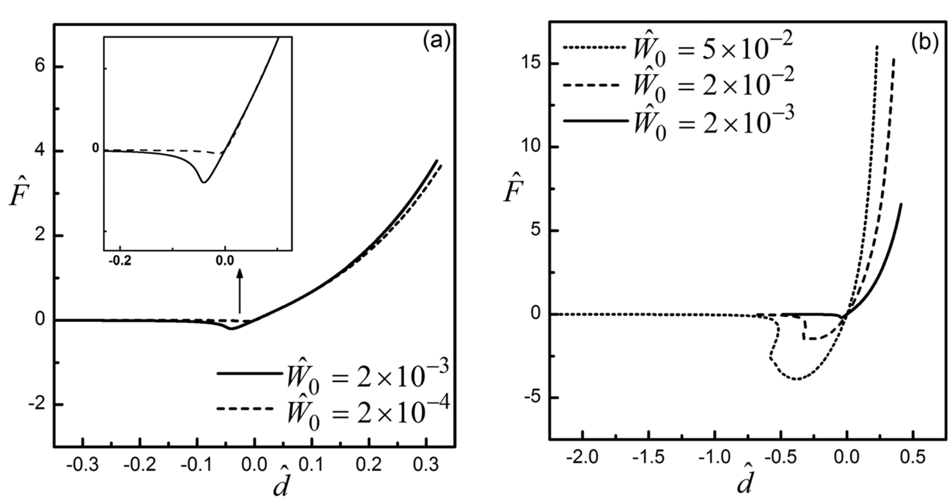

FIG. 15. [(a) and (b)] Effect of adhesive per unit area energy $\left(\hat{W}_0\right)$ in dimensionless f-d curves. Comparison between (a) weak $\hat{W}_0 = 2\times10^{-4},\ 2\times10^{-3}$ and (b) strong $\hat{W}_0 = 5\times10^{-2},\ 2\times10^{-2}$ adhesion cases. The rest of simulation parameters are $\hat{P}_A = 3$ and $\hat{k}_b = 2.7\times10^{-3}$ for all of the curves.

them, provides a reliable means to estimate the interaction potential between the shell and cantilever. This can be combined with the evolution of the f-d curve in order to provide estimates of the shell area dilatation and bending stiffness. A preliminary study based on a standard methodology with a point load[26] does not accurately reproduce experimental f-d measurements in the buckled regime and in the regime of dominant gas compression. Therefore, application of the present model to this end is a promising alternative that is left for a future study.

Another important aspect of the static response as the interaction potential increases pertains to the details of the f-d curve and the associated shapes and load distribution on the shell. As illustrated by Figs. 15(a) and 15(b), for increasing values of the interaction potential, the f-d curve exhibits a gradual deviation from the Reissner slope while the ensuing nonlinear curved upwards regime weakens in favor of a quadratic, Fig. 15(a), or almost linear response pattern, Fig. 15(b), with a larger slope than the one predicted for the classical Reissner regime. As can be surmised based on Figs. 16 and 17, this tendency is a result of the increased resistance to film thinning with increasing adhesion of the shell on the cantilever and the corresponding tendency of continuous elongation of the contact region as opposed to increasing gas compression. In particular, Figs. 16(b) and 17(b) show the energy distribution where the increased importance of gas-compression over bending but, primarily, the dominant effect of stretching and interaction potential is evident in this process. Furthermore, the distribution of disjoining pressure is shown in Figs. 16(c) and 17(c) as a function of increasing relative deformation, where it is seen that the contribution from the transition layer is subdominant to that from the contact region. In particular, there is a competition between the increase in the repulsive force through thinning of the film in the contact region and via elongation of the contact region. The former results in gas compression and compression of the main part of the shell, and it is also responsible for the cubic dependence of the force on deformation. The latter results in the intensification of the in-plane compressive stresses in the contact region and is responsible for the linear dependence of the force on deformation. As the interaction potential increases, the latter component dominates, thus generating a linear response pattern with a larger slope than the Reissner regime due to the increased deviation from sphericity as a result of the progressive elongation of the contact region. This effect was pointed out in the section dedicated to the asymptotic structure of the solution depending on the dominant force balance, where the shear stress resultant in the transition region determines the compressive in-plane stress at the junction between the transition and contact regions and subsequently produces the linear dependence on the deformation. This is especially true in Fig. 17(c) where the load almost

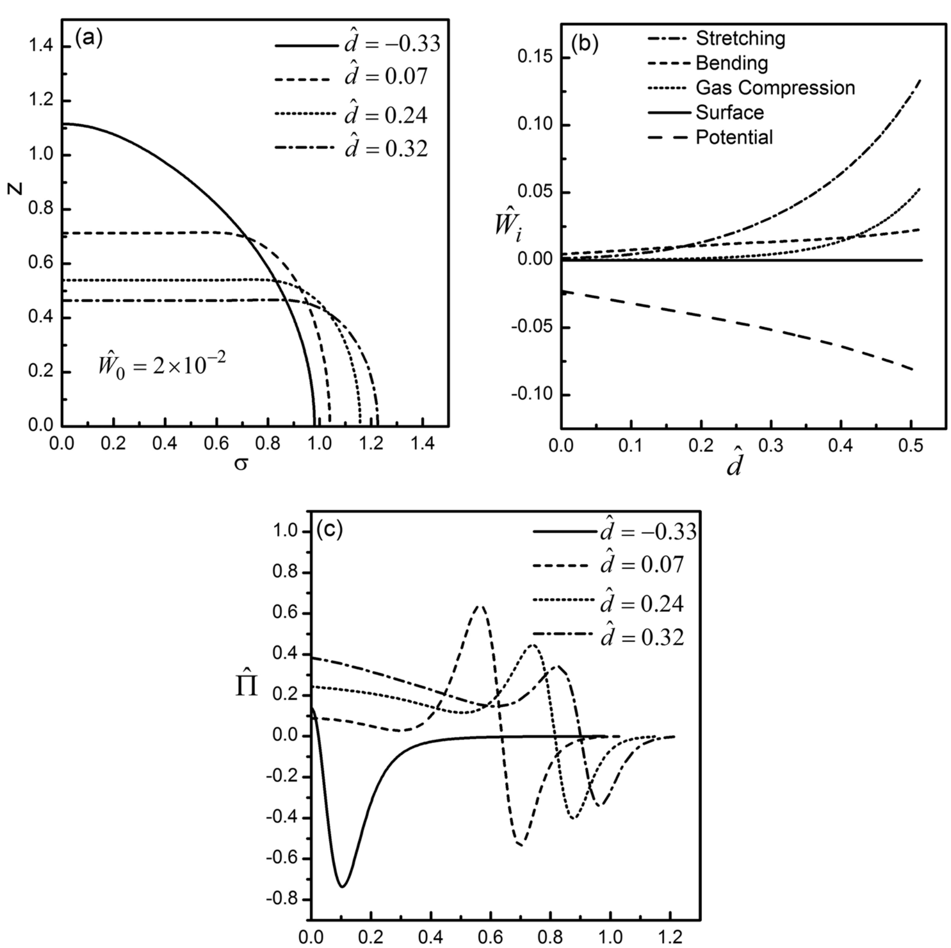

FIG. 16. Evolution of (a) shapes, (b) dimensionless energy components $\hat{W}_i$ as a function of dimensionless deformation $\hat{d}$, and (c) dimensionless disjoining pressure profiles $\hat{\Pi}$ as a function of the radial coordinate σ for different values of deformation, which correspond to strong adhesion. The simulation parameters are $\hat{k}_b = 2.7\times10^{-3}$, $\hat{P}_A = 3$, $\hat{W}_0 = 2\times10^{-2}$.

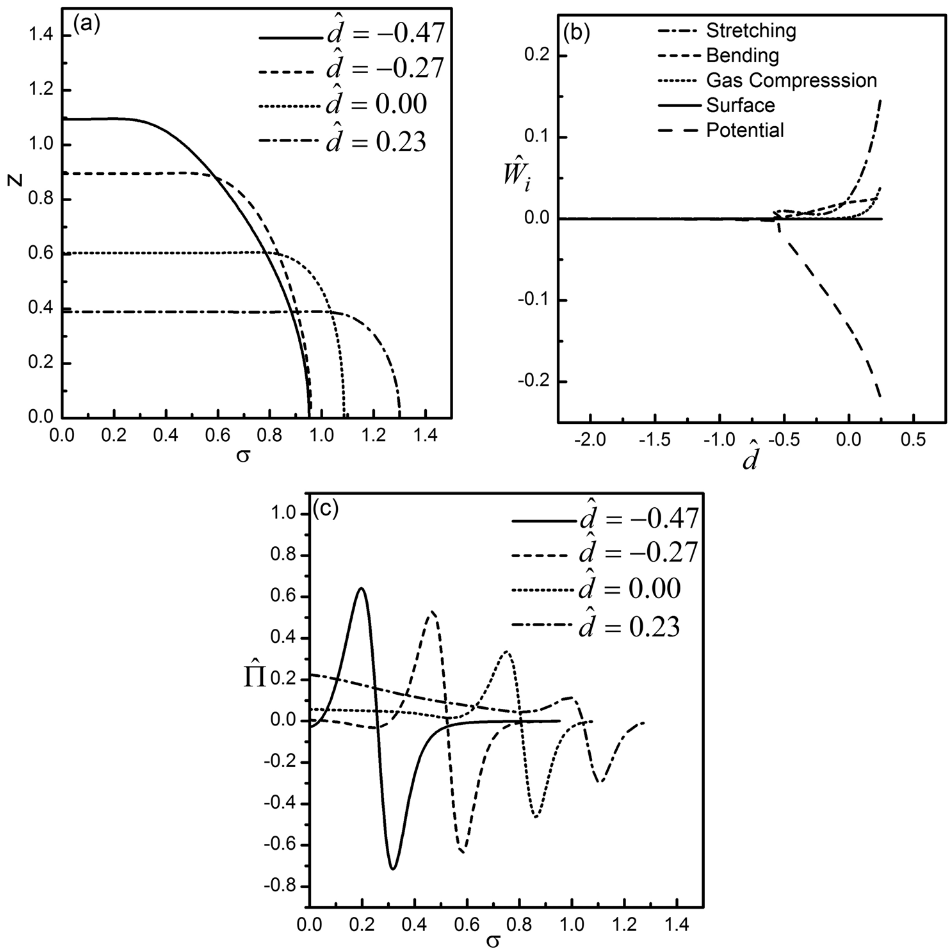

FIG. 17. Evolution of (a) shapes, (b) dimensionless energy components $\hat{W}_i$ as a function of dimensionless deformation $\hat{d}$, and (c) dimensionless disjoining pressure profiles $\hat{\Pi}$ as a function of radial coordinate σ for different values of deformation, which correspond to strong adhesion. The simulation parameters are $\hat{k}_b = 2.7 \times 10^{-3}$; $\hat{P}_A = 3$, $\hat{W}_0 = 5 \times 10^{-2}$.

vanishes in the contact region due to the very large interaction potential. Consequently, a very narrow load distribution emerges at the edge of the contact region, in a fashion that is similar to the Reissner regime that gives rise to a linear response in the f-d curve. As was discussed in the context of the response of hard shells this trend was a recurring theme in the present study, whenever a linear response pattern was revealed by the simulations with significant deviations from the Reissner slope.

AFM experiments and clinical applications of MBs are performed in an aqueous environment; thus, surface tension between the shell coating and water is a parameter that requires investigation, especially when we wish to characterize the nature of the coating, i.e., if it is a viscoelastic solid or liquid. In addition, consideration of surface tension even for a solid coating might simulate possible defects on the shell, like holes, where we have a gas-water interface. The static response of coated MBs is mainly investigated in the context of classic shell mechanics,[23,47] where the surface tension is not accounted for. In a recent study[59] on the synthesis and development of MBs covered with phospholipid monolayers, it was reported that the surface tension of such coatings is very small or even near zero, $\gamma_{BW} \sim 10^{-3}$ N/m, while an older study[60] also suggested that surface tension in lipid monolayer membranes is around 10^{-3} N/m. We consider two cases here with $\gamma_{BW} = 4 \times 10^{-3}$ and 4×10^{-2} N/m, i.e., $\hat{\gamma}_{BW} = 8 \times 10^{-2}$ and 8×10^{-1}, for our simulation and the rest of parameters the same as in Fig. 7. Figure 18 demonstrates that surface tension significantly increases the required force for the same

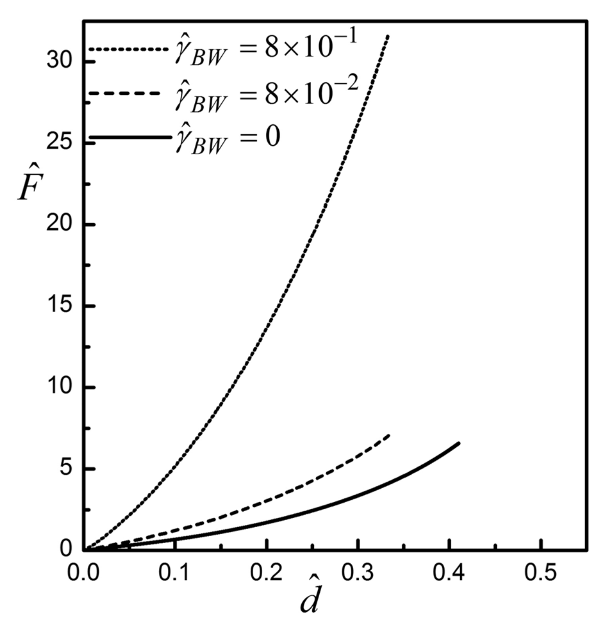

FIG. 18. Dimensionless force $\hat{F}$ as a function of dimensionless deformation $\hat{d}$ for different values of dimensionless surface tension $\hat{\gamma}_{BW}$. The rest of the simulation parameters are $\hat{k}_b = 2.7 \times 10^{-3}$, $\hat{P}_A = 3$, $\hat{W}_0 = 2 \times 10^{-3}$.

deformation or, alternatively, surface tension adds an extra resistance on the shell. In particular, surface tension is an isotropic property that acts on the shell along with the in-plane stresses τ_{ss} and $\tau_{\varphi\varphi}$, which depend on the direction. Thus, surface tension could be interpreted as the isotropic part of the in-plane stress tensor. This argument implies that surface energy consists of an isotropic part, namely, surface tension, and the purely elastic part that depends on the extent of local deformation. In addition, Eqs. (20) imply that when the shell/liquid interface is characterized by surface tension the gas pressure is higher than the ambient by the term of $2\gamma_{BW}k_m$, i.e., the capillary pressure. The latter introduces an additional stiffness component in the interfacial force balance and renders gas compression a more energy consuming part in the equilibrium process; see also Fig. 19(b) where the relative importance of the different energy components is plotted against relative deformation when $\hat{\gamma}_{BW} = 8 \times 10^{-2}$. As a result, the validity of the Reissner regime shrinks within a smaller window of relative deformations; see also the f-d curve in Fig. 18 for the case with $\hat{\gamma}_{BW} = 8 \times 10^{-2}$ exhibiting a cubic response pattern for large deformations. Figures 19(a)–19(c) corroborate this behavior in the evolution of the shell shape, energy distribution, and disjoining pressure in a manner that is similar to the case with $\gamma_{BW} = 0$ shown in Fig. 7 but with larger contribution to total energy due to volume compression.

Finally, the static response pattern for an even larger value of surface tension, $\hat{\gamma}_{BW} = 8 \times 10^{-1}$, is shown in terms of the f-d curve in Fig. 18 and the evolution of the shape, energy, and load distribution with relative deformation is shown in Figs. 20(a)–20(c). The registered response pattern resembles the one obtained with increasing interaction potential where an almost flat and repulsive disjoining pressure distribution develops in the contact region as can be verified by cross-examining Figs. 17(c) and 20(c). In the latter graph, a strong and almost flat repulsive force is registered within the contact region, even at nearly zero deformation, as a result of the capillary pressure of the microbubble. This is in contrast to the almost point load distribution obtained in the case presented in Fig. 17(c) leading to a linear f-d curve, at least in the initial part before the resistance to volume compression dominates shell rigidity. It is due to the dominant resistance to film thinning that is exhibited by the shell when surface tension increases, which enhances elongation of the contact region instead of volume compression, see also Fig. 20(a), and the corresponding stretching and potential vs gas compression components in the energy distribution, Fig. 20(b). In this fashion, the f-d curve assumes an almost quadratic or even linear form depending on the ratio between surface tension and area dilatation, Fig. 18. This is a pattern that distinguishes shells with significant surface tension from purely elastic shells and may play a role in the estimation of their mechanical properties.

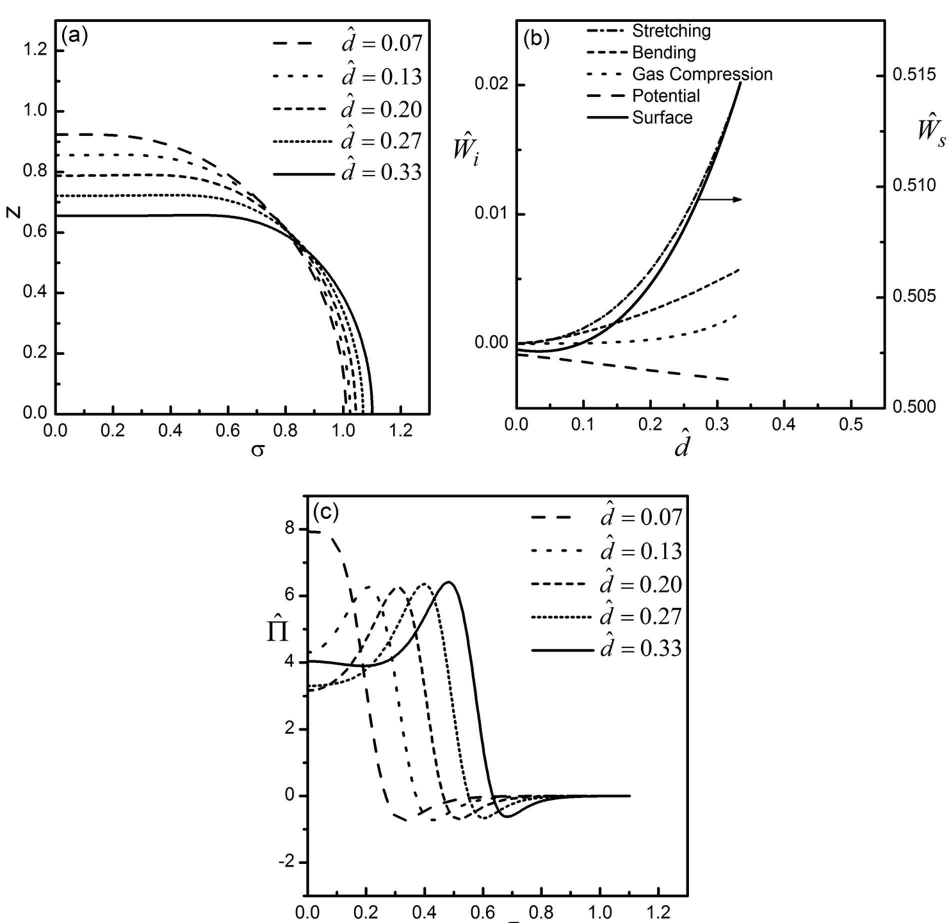

FIG. 19. Evolution of (a) shapes, (b) dimensionless energy components $\hat{W}_i$ (the energy due to surface tension, $\hat{W}_s$, is on the right axis) as a function of dimensionless deformation $\hat{d}$, and (c) dimensionless disjoining pressure profiles $\hat{\Pi}$ as a function of the radial coordinate σ for different values of deformation. The simulation parameters are $\hat{k}_b = 2.7 \times 10^{-3}$, $\hat{P}_A = 3$, $\hat{W}_0 = 2 \times 10^{-3}$, $\hat{\gamma}_{BW} = 8 \times 10^{-2}$.

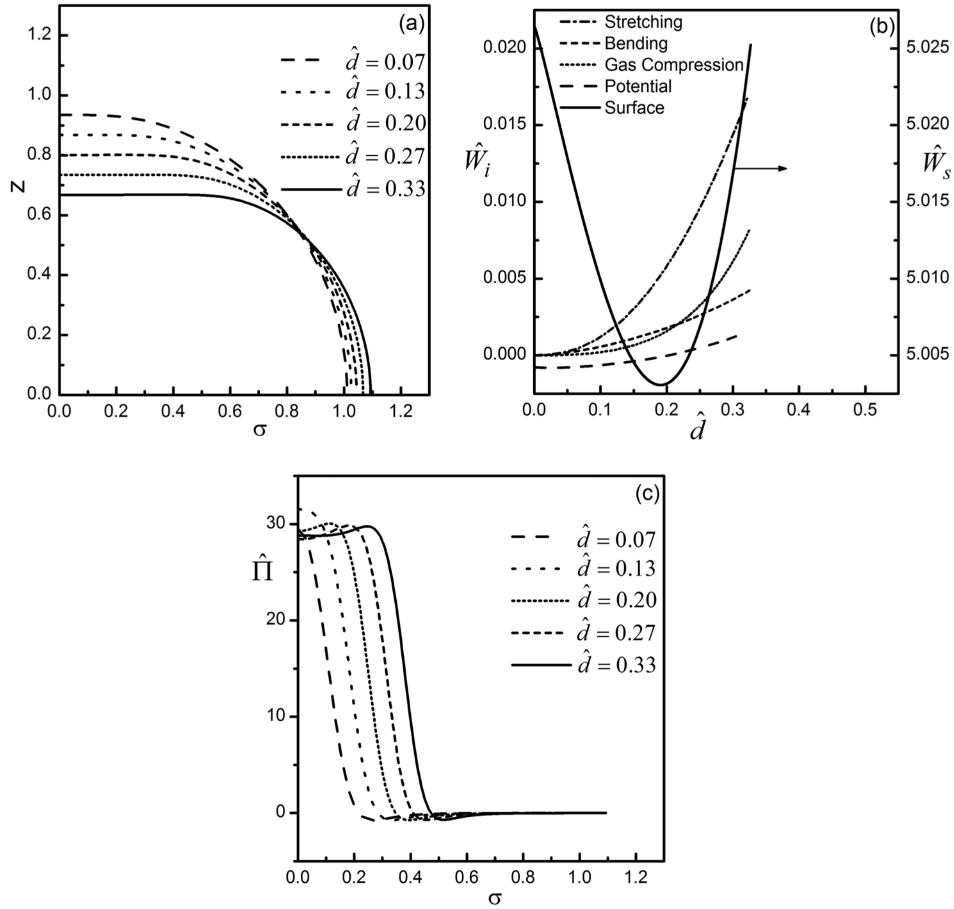

FIG. 20. Evolution of (a) shapes, (b) dimensionless energy components $\hat{W}_i$ (the energy due to surface tension, $\hat{W}_s$, is on the right axis) as a function of dimensionless deformation $\hat{d}$, and (c) dimensionless disjoining pressure profiles $\hat{\Pi}$ as a function of the radial coordinate σ for different values of deformation. The simulation parameters are $\hat{k}_b = 2.7 \times 10^{-3}$, $\hat{P}_A = 3$, $\hat{W}_0 = 2 \times 10^{-3}$, $\hat{\gamma}_{BW} = 8 \times 10^{-1}$.

VI. CONCLUDING REMARKS

A novel methodology was developed for the investigation of the static response of coated microbubbles that are compressed by two rigid planes. Ultimately it is desired to simulate afm measurements on microbubbles coated with hard polymeric or soft phospholipid shells in order to recover the elastic properties of the shell. In both cases, due to the hydrophilic nature of the involved surfaces, an ultrathin aqueous film separates the shell from the cantilever that acts as a mediator of the load exerted by the latter on the former surface. The intensity of this interaction is very important for the type of response that will be observed, and in the present study, it is modeled via a long range attractive, short range repulsive potential that gives rise to a disjoining pressure that repels the shell interface as the distance from the cantilever decreases below a characteristic length scale. In this fashion, a smooth load distribution is generated that allowed us to capture a wide range of different response patterns. Stretching strains are also accounted for in the context of Hookean and strain softening constitutive laws, the latter introducing nonlinearity in the static response by hardening the shell material at compression, and bending strains via a linear relationship that relates the curvature at rest and during deformation. Finally, gas compressibility and shell/liquid interfacial tension are also introduced in order to complete the set of stiffnesses that comprise the microbubble's resistance to deformation during equilibrium. The finite element methodology with b-cubic splines as basis functions, in order to accommodate bending strains, is applied for capturing shell deformation at external loads of increasing intensity and varying distribution.

In particular, the dimensionless pressure, $\hat{P}_A$, was used as a parameter that distinguishes hard, $\hat{P}_A << 1$, from soft shells, $\hat{P}_A \approx 1$, and the corresponding main response patterns that were obtained. In the former case, the simulated f-d curves exhibited the standard linear to curved downwards transition from flat to buckled shapes corresponding to the Reissner and Pogorelov regimes, respectively. Decreasing the dimensionless bending resistance, $\hat{k}_b$, enhances the onset of buckling by making bending an energetically favorable component of the energy distribution. In terms of the modeling approach of the present study, the above two regimes are characterized by the load concentrating at the edge of the contact region and within a dimpled region where most of the bending strain develops, called transition region, respectively. The latter region smoothly joins the contact region with the shell outer part and is the part of the shell where intermolecular forces directly balance bending. Consequently, the above two regimes signify dominance of the stretching and bending strains that are generated as a result of the external load in the contact and transition layers, respectively.

Soft shells, $\hat{P}_A \approx 1$, exhibit a different static response with the classic linear Reissner regime followed by a curved upwards nonlinear regime that is characterized by a cubic dependence of force on deformation. In the latter regime, the dominant balance is between pressure drop and stretching throughout the outer part of the shell. The force on the shell in this case is mainly due to the repulsive force that develops throughout the contact region, thus forcing compression of the gas enclosed in the microbubble. Such a regime exists for hard shells as well, albeit in the post-buckling regime and at quite large deformations for which a significant volume compression has already taken place. In the case of soft shells, however, buckling is bypassed by volume compression that is energetically favorable. In fact, as bending resistance, $\hat{k}_b$, increases, the above pattern is enhanced and the range of validity of the Reissner regime extends to higher deformations.

When shell adhesion constitutes a significant stiffness component of the equilibrium process, i.e., as $\hat{W}_0$ increases, compression of the ultrathin film that separates the shell from the cantilever is not energetically favorable and significant elongation of the contact region takes place signifying the onset of compressive in-plane stresses, mainly, and bending. As a result, volume compression and the onset of the cubic regime subside and, as deviation from sphericity intensifies, an almost quadratic response pattern emerges. In fact, for large values of the adhesion potential, a similar load distribution to the Reissner response pattern develops, with the load concentrated at the edge of the contact region. In this case, a linear response is observed with a slope that is different from the one predicted by Reissner, reflecting the departure of the shell shape from sphericity. Increasing the interfacial tension between the shell and surrounding liquid, i.e., as $\hat{\gamma}_{BW}$ increases, produces similar effects in the sense that it generates an additional stiffness component, namely, capillary pressure, that impairs the capability of the shell volume to compress and facilitates elongation of the contact regime. As a result, a response pattern that is almost quadratic is exhibited, instead of the typical cubic response that characterizes the importance of interfacial tension.

Finally, simulations with a strain softening constitutive law gave the same response pattern for both types of materials. Deviations have been observed albeit for unrealistic high deformations, where axisymmetry and the elastic behavior assumption are anticipated to lose validity. This result is attributed to the fact that the contact region is usually compressed, while the main part of the shell is elongated, and consequently, the effect of the constitutive law is mitigated. Simulations that we have performed for similar type shells subject to a uniform pressure respond differently, depending on the shell constitutive law, as in these cases the shell is uniformly compressed until buckling takes place.

The above methodology is a comprehensive tool for the study of contact problems when elastic shells interact with hydrophilic interfaces. In particular, and depending on the affinity between the shell and cantilever materials, the maximum attraction or pull-off force that is measured during an experiment can serve as a means to estimate the interaction potential, w_0, which can be then used for simulating this process. Furthermore, it is proposed that combination of the linear Reissner regime with, either the nonlinear curved down post-buckling regime in the case of hard polymeric shells or the nonlinear cubic regime, in the case of soft phospholipid shells, can be used to recover area dilatation and bending resistance from simulated or experimentally obtained force deformation curves. A preliminary comparison of the present model with afm experiments provided in Figs. 5(a) and 5(b) of the benchmark Sec. III B shows satisfactory agreement for both types of coatings, i.e., polymers and phospholipids. An extensive comparison with available afm measurements from the literature, using the methodology for parameter estimation that was outlined in Sec. IV in the context of the asymptotic analysis, will be performed in a future study in order to validate the importance of the physical mechanisms that are incorporated in the model proposed in the present study.

ACKNOWLEDGMENTS

The present research was performed in the framework of the operational program "Education and lifelong learning"-"Aristeia-CONTAGEUSNUMSTADY" and was cofounded by the European Union (European Social Fund) and national resources. The authors wish also to thank Professor V. Koutsos and Professor V. Sboros for fruitful discussions on AFM experiments. In addition, valuable suggestions and discussions on contact mechanics by Professor A. Giannakopoulos are gratefully acknowledged.

APPENDIX: DERIVATION OF DISJOINING PRESSURE USING CALCULUS OF VARIATIONS

The energy due to intermolecular forces is $W_{\text{int}} = \oiint_A w_{\text{int}} dA$; therefore, its variation for an axisymmetric shell in cylindrical (σ, z, φ) coordinates is

$$\begin{aligned}\delta W_{\text{int}} &= \oiint_A \vec{\nabla} w_{\text{int}} \cdot \delta\vec{r}\, dA + \oiint_A w_{\text{int}} \frac{\delta(dA)}{\delta\vec{r}} \cdot \delta\vec{r} \\ &= \int_0^1 2\pi \vec{\nabla} w_{\text{int}} \sigma \sqrt{\sigma_\xi^2 + z_\xi^2} \cdot \delta\vec{r}\, d\xi \\ &\quad + \int_0^1 2\pi w_{\text{int}} \frac{\delta\left(\sigma\sqrt{\sigma_\xi^2 + z_\xi^2}\right)}{\delta\vec{r}} \cdot \delta\vec{r}\, d\xi. \end{aligned} \quad \text{(A1)}$$

Noting that $\vec{t}_s = \sigma_s \vec{e}_\sigma + z_s \vec{e}_z$, $\vec{n} = \sigma_s \vec{e}_z - z_s \vec{e}_\sigma$, the first term assumes the form

$$\vec{\nabla} w_{\text{int}} = \underbrace{\cancel{\frac{\partial w_{\text{int}}}{\partial \sigma}}}_{0} \vec{e}_\sigma + \frac{\partial w_{\text{int}}}{\partial z} \vec{e}_z = \frac{\partial w_{\text{int}}}{\partial z} \vec{e}_z = \frac{\partial w_{\text{int}}}{\partial z}\left(z_s \vec{t}_s + \sigma_s \vec{n}\right) = \frac{\partial w_{\text{int}}}{\partial s} \vec{t}_s + \frac{\partial w_{\text{int}}}{\partial n} \vec{n}. \quad \text{(A2)}$$

Employing the general rule of variation,[61] $\delta F(x, y, x', y') = \frac{\partial F}{\partial x}\delta x + \frac{\partial F}{\partial y}\delta y + \frac{\partial F}{\partial x'}\delta x' + \frac{\partial F}{\partial y'}\delta y'$, $()' = \frac{d}{d\xi}$, where ξ is an independent parameter that does not vary; the variation of the metric becomes

$$\delta g=\int_0^1 2\pi w_{\mathrm{int}}\frac{\delta\left(\sigma\sqrt{\sigma_\xi^2+z_\xi^2}\right)}{\delta\vec{r}}d\xi=\int_0^1 2\pi\left[w_{\mathrm{int}}\sqrt{\sigma_\xi^2+z_\xi^2}\delta\sigma+w_{\mathrm{int}}\sigma\frac{1}{2}\frac{2\sigma_\xi}{\sqrt{\sigma_\xi^2+z_\xi^2}}\delta\sigma_\xi+w_{\mathrm{int}}\sigma\frac{1}{2}\frac{2z_\xi}{\sqrt{\sigma_\xi^2+z_\xi^2}}\delta z_\xi\right]d\xi$$

$$=\int_0^1 2\pi\left[w_{\mathrm{int}}\sqrt{\sigma_\xi^2+z_\xi^2}\delta\sigma-\frac{d}{d\xi}\left(\frac{\sigma\sigma_\xi w_{\mathrm{int}}}{\sqrt{\sigma_\xi^2+z_\xi^2}}\right)\delta\sigma-\frac{d}{d\xi}\left(\frac{\sigma z_\xi w_{\mathrm{int}}}{\sqrt{\sigma_\xi^2+z_\xi^2}}\right)\delta z\right]d\xi+\underbrace{\left.\left(\frac{2\pi\sigma\sigma_\xi w_{\mathrm{int}}}{\sqrt{\sigma_\xi^2+z_\xi^2}}\delta\sigma+\frac{2\pi\sigma z_\xi w_{\mathrm{int}}}{\sqrt{\sigma_\xi^2+z_\xi^2}}\delta z\right)\right|_0^1}_{=0\text{ for a closed body}}\Rightarrow$$

$$\delta g=\int_0^1 2\pi w_{\mathrm{int}}\sqrt{\sigma_\xi^2+z_\xi^2}\delta\sigma d\xi$$

$$+\int_0^1 2\pi\left[\left(-\frac{\sigma\sigma_\xi}{\sqrt{\sigma_\xi^2+z_\xi^2}}\frac{dw_{\mathrm{int}}}{d\xi}-w_{\mathrm{int}}\frac{\left(\sigma_\xi^2+\sigma\sigma_{\xi\xi}\right)\left(\sigma_\xi^2+z_\xi^2\right)-\sigma\sigma_\xi\left(\sigma_\xi\sigma_{\xi\xi}+z_\xi z_{\xi\xi}\right)}{\left(\sigma_\xi^2+z_\xi^2\right)^{3/2}}\right)\delta\sigma\right]d\xi$$

$$+\int_0^1 2\pi\left[\left(-\frac{\sigma z_\xi}{\sqrt{\sigma_\xi^2+z_\xi^2}}\frac{dw_{\mathrm{int}}}{d\xi}-w_{\mathrm{int}}\frac{\left(\sigma_\xi z_\xi+\sigma z_{\xi\xi}\right)\left(\sigma_\xi^2+z_\xi^2\right)-\sigma z_\xi\left(\sigma_\xi\sigma_{\xi\xi}+z_\xi z_{\xi\xi}\right)}{\left(\sigma_\xi^2+z_\xi^2\right)^{3/2}}\right)\delta z\right]d\xi. \tag{A3}$$

The integrals in (A3) represent the components of a vector in σ and z direction, which has the following form: $\int_0^1(A_\sigma\delta\sigma+A_z\delta z)\,d\xi=\int_0^1(A_\sigma\vec{e}_\sigma+A_z\vec{e}_z)\cdot(\delta\sigma\vec{e}_\sigma+\delta z\vec{e}_z)\,d\xi=\int_0^1\vec{A}\cdot\delta\vec{r}d\xi$. Alternatively, it is possible to express $\vec{A}$ in the normal (n) and tangential (s) directions $\vec{A}=A_n\vec{n}+A_s\vec{t}_s$ by taking the inner products $\vec{A}\cdot\vec{n}$, $\vec{A}\cdot\vec{t}_s$, and add the result to Eq. (A1) containing the variation of the interaction potential W_{int}. Consequently, the above integral formally reads as

$$\delta g=\int_0^1\left(A_n\vec{n}+A_s\vec{t}\right)\cdot\delta\vec{r}d\xi, \tag{A4}$$

and in the following, we proceed to obtain $\mathrm{A_n}$ and $\mathrm{A_s}$:

$$A_s=-2\pi\sigma\frac{dw_{\mathrm{int}}}{ds}\sqrt{\sigma_\xi^2+z_\xi^2}+2\pi w_{\mathrm{int}}\left[\frac{\sigma_\xi\left(\sigma_\xi^2+z_\xi^2\right)^2-\sigma_\xi\left(\sigma_\xi^2+\sigma\sigma_{\xi\xi}\right)\left(\sigma_\xi^2+z_\xi^2\right)+\sigma\sigma_\xi^2\left(\sigma_\xi\sigma_{\xi\xi}+z_\xi z_{\xi\xi}\right)}{\left(\sigma_\xi^2+z_\xi^2\right)^2}\right]$$

$$+2\pi w_{\mathrm{int}}\left[\frac{-z_\xi\left(\sigma_\xi z_\xi+\sigma z_{\xi\xi}\right)\left(\sigma_\xi^2+z_\xi^2\right)+\sigma z_\xi^2\left(\sigma_\xi\sigma_{\xi\xi}+z_\xi z_{\xi\xi}\right)}{\left(\sigma_\xi^2+z_\xi^2\right)^2}\right]=-2\pi\sigma\frac{dw_{\mathrm{int}}}{ds}\sqrt{\sigma_\xi^2+z_\xi^2}$$

$$+2\pi w_{\mathrm{int}}\frac{\overbrace{\left(\sigma_\xi^2+z_\xi^2\right)\left[\sigma_\xi\left(\sigma_\xi^2+z_\xi^2\right)-\sigma_\xi\left(\sigma_\xi^2+\sigma\sigma_{\xi\xi}\right)-z_\xi\left(\sigma_\xi z_\xi+\sigma z_{\xi\xi}\right)+\sigma\left(\sigma_\xi\sigma_{\xi\xi}+z_\xi z_{\xi\xi}\right)\right]}^{=0}}{\left(\sigma_\xi^2+z_\xi^2\right)^2}\Rightarrow$$

$$A_s=-2\pi\frac{dw_{\mathrm{int}}}{ds}\sqrt{\sigma_\xi^2+z_\xi^2}\sigma. \tag{A5}$$

In the same way, the projection in the normal direction is

$$
\begin{aligned}
A_n &= 2\pi \frac{dw_{\text{int}}}{d\xi} \frac{\sigma \overbrace{\left(\sigma_\xi z_\xi - z_\xi \sigma_\xi\right)}^{=0}}{\sqrt{\sigma_\xi^2 + z_\xi^2}} \frac{d\xi}{ds} + 2\pi \frac{d\xi}{ds} \left[-w_{\text{int}} z_\xi \sqrt{\sigma_\xi^2 + z_\xi^2} + w_{\text{int}} z_\xi \frac{\left(\sigma_\xi^2 + \sigma\sigma_{\xi\xi}\right)\left(\sigma_\xi^2 + z_\xi^2\right) - \sigma\sigma_\xi \cancel{\left(\sigma_\xi \sigma_{\xi\xi} + z_\xi z_{\xi\xi}\right)}}{\left(\sigma_\xi^2 + z_\xi^2\right)^{3/2}} \right] \\
&\quad - 2\pi w_{\text{int}} \frac{d\xi}{ds} \sigma_\xi \frac{\left(\sigma_\xi z_\xi + \sigma z_{\xi\xi}\right)\left(\sigma_\xi^2 + z_\xi^2\right) - \sigma z_\xi \cancel{\left(\sigma_\xi \sigma_{\xi\xi} + z_\xi z_{\xi\xi}\right)}}{\left(\sigma_\xi^2 + z_\xi^2\right)^{3/2}} \\
&= 2\pi w_{\text{int}} \frac{d\xi}{ds} \sigma \sqrt{\sigma_\xi^2 + z_\xi^2} \left[-\frac{z_\xi}{\sigma} + \frac{\sqrt{\sigma_\xi^2 + z_\xi^2} \left[z_\xi \left(\cancel{\sigma_\xi^2} + \sigma\sigma_{\xi\xi}\right) - \sigma_\xi \left(\cancel{\sigma_\xi z_\xi} + \sigma z_{\xi\xi}\right)\right]}{\sigma\left(\sigma_\xi^2 + z_\xi^2\right)^{3/2}} \right] \\
&= 2\pi w_{\text{int}} \sigma \sqrt{\sigma_\xi^2 + z_\xi^2} \left[-\frac{z_\xi}{\sigma\sqrt{\sigma_\xi^2 + z_\xi^2}} + \frac{\sigma_{\xi\xi} z_\xi - \sigma_\xi z_{\xi\xi}}{\left(\sigma_\xi^2 + z_\xi^2\right)^{3/2}} \right] = 2\pi w_{\text{int}} \left[\underbrace{-\frac{z_s}{\sigma\sqrt{\sigma_s^2 + z_s^2}}}_{k_s} + \underbrace{\frac{\sigma_{ss} z_s - \sigma_s z_{ss}}{\left(\sigma_s^2 + z_s^2\right)^{3/2}}}_{k_\varphi} \right] \sigma \Rightarrow \\
A_n &= 2\pi w_{\text{int}} \sigma \sqrt{\sigma_\xi^2 + z_\xi^2}\, 2k_m.
\end{aligned} \tag{A6}
$$

Thus, substituting (A2), (A5), and (A6) into (A1),

$$
\begin{aligned}
\delta W_{\text{int}} &= \oiint_A \left(\frac{\partial w_{\text{int}}}{\partial s} \vec{t} + \frac{\partial w_{\text{int}}}{\partial n} \vec{n} \right) \cdot \delta\vec{r} dA \\
&\quad + \oiint_A \left(-\frac{dw_{\text{int}}}{ds} \vec{t} + w_{\text{int}} 2k_m \vec{n} \right) \cdot \delta\vec{r} dA \Rightarrow
\end{aligned}
$$

$$
\delta W_{\text{int}} = \oiint_A \left(\frac{\partial w_{\text{int}}}{\partial n} + 2k_m w_{\text{int}} \right) \vec{n} \cdot \delta\vec{r} dA. \tag{A7}
$$

Consequently, the total force exerted on the shell as a result of the compression of the liquid film is provided by Eq. (18),

$$
\vec{F} = -\frac{\delta W_{\text{int}}}{\delta \vec{r}} = \oiint_A \left(-\frac{\partial w_{\text{int}}}{\partial n} - 2k_m w_{\text{int}} \right) \vec{n} dA. \tag{A8}
$$

[1] B. A. Kaufmann, K. Wei, and J. R. Lindner, "Contrast echocardiography," Curr. Probl. Cardiol. **32**, 51 (2007).
[2] A. Stanziola, M. Toulemonde, Y. O. Yildiz, R. J. Eckersley, and M. X. Tang, "Ultrasound imaging with microbubbles (life sciences)," IEEE Signal Process. Mag. **33**, 111 (2016).
[3] K. Ferrara, R. Pollard, and M. Borden, "Ultrasound microbubble contrast agents: Fundamentals and application to gene and drug delivery," Annu. Rev. Biomed. Eng. **9**, 415 (2007).
[4] K. Kooiman, H. J. Vos, M. Versluis, and N. de Jong, "Acoustic behavior of microbubbles and implications for drug delivery," Adv. Drug Delivery Rev. **72**, 28 (2014).
[5] A. L. Klibanov, "Ligand-carrying gas-filled microbubbles: Ultrasound contrast agents for targeted molecular imaging," Bioconjugate Chem. **16**, 9 (2005).
[6] V. Sboros, "Response of contrast agents to ultrasound," Adv. Drug Delivery Rev. **60**, 1117 (2008).
[7] M. Emmer, A. van Wamel, E. Goertz, and N. de Jong, "The onset of microbubble vibration," Ultrasound Med. Biol. **33**, 941 (2007).
[8] S. Qin and K. W. Ferrara, "The natural frequency of nonlinear oscillation of ultrasound contrast agents in microvessels," Ultrasound Med. Biol. **33**, 1140 (2007).
[9] K. Tsiglifis and N. A. Pelekasis, "Nonlinear radial oscillations of encapsulated microbubbles subject to ultrasound: The effect of membrane constitutive law," J. Acoust. Soc. Am. **123**, 4059 (2008).
[10] D. H. Thomas, P. Looney, R. Steel, N. Pelekasis, W. N. McDicken, T. Anderson, and V. Sboros, "Acoustic detection of microbubble resonance," Appl. Phys. Lett. **94**, 243902 (2009).
[11] S. M. van der Meer, B. Dollet, M. M. Voormolen, C. T. Chin, A. Bouakaz, N. de Jong, M. Versluis, and D. Lohse, "Microbubble spectroscopy of ultrasound contrast agents," J. Acoust. Soc. Am. **121**, 648 (2007).
[12] S.-Y. Wu, C. C. Chen, Y.-S. Tung, O. O. Olumolade, and E. E. Konofagou, "Effects of the microbubble shell physicochemical properties on ultrasound-mediated drug delivery to the brain," J. Controlled Release **212**, 30 (2015).
[13] T. J. A. Kokhuis, V. Garbin, K. Kooiman, B. A. Naaijkens, L. J. M. Juffermans, O. Kamp, A. F. W. van der Steen, M. Versluis, and N. de Jong, "Secondary Bjerknes forces deform targeted microbubbles," Ultrasound Med. Biol. **39**(3), 490 (2013).
[14] P. Marmottant, A. Bouakaz, N. de Jong, and C. Quilliet, "Buckling resistance of solid shell bubbles under ultrasound," J. Acoust. Soc. Am. **129**, 1231 (2011).
[15] M. Overvelde, "Ultrasound contrast agents-dynamics of coated microbubbles," Ph.D Thesis, University of Twente, 2010, https://research.utwente.nl/en/publications/ultrasound-contrast-agents-dynamics-of-coated-bubbles-2.
[16] K. Tsigklifis and N. A. Pelekasis, "Simulations of insonated contrast agents: Saturation and transient break-up," Phys. Fluids **25**, 032109 (2013).
[17] M. Vlachomitrou and N. Pelekasis, "Dynamic simulation of a coated microbubble in an unbounded flow: Response to a step change in pressure," J. Fluid Mech. **822**, 717 (2017).
[18] D. Chatterjee and K. Sarkar, "A Newtonian rheological model for the interface of microbubble contrast agents," Ultrasound Med. Biol. **29**, 1749 (2003).
[19] W. Wang, C. C. Moser, and M. A. Wheatley, "Langmuir trough study of surfactant mixtures used in the production of a new ultrasound contrast agent consisting of stabilized microbubbles," J. Phys. Chem. **100**, 13815 (1996).
[20] V. V. Lulevich, D. Andrienko, and O. I. Vinogradova, "Elasticity of polyelectrolyte multilayer microcapsules," J. Chem. Phys. **120**, 3822 (2004).
[21] M. E. R. Shanahan, "A novel test for the appraisal of solid/solid interfacial interactions," J. Adhes. **63**, 15 (1997).
[22] N. Elsner, F. Dubreuil, R. Weinkamer, M. Wasicek, F. D. Fischer, and A. Fery, *Mechanical Properties of Freestanding Polyelectrolyte Capsules: A Quantitative Approach Based on Shell Theory* (Springer Berlin Heidelberg, Berlin, Heidelberg, 2006).

[23]E. Reissner, "Stresses and small displacements of shallow spherical shells. II," J. Math. Phys. **25**, 279 (1946).
[24]A. V. Pogorelov, *Bendings of Surfaces and Stability of Shells* (American Mathematical Society, 1988).
[25]E. Glynos, V. Koutsos, W. N. McDicken, C. M. Moran, S. D. Pye, J. A. Ross, and V. Sboros, "Nanomechanics of biocompatible hollow thin-shell polymer microspheres," Langmuir **25**, 7514 (2009).
[26]A. Lytra, N. Pelekasis, V. Sboros, E. Glynos, and V. Koutsos, "Static response of coated microbubbles: Modeling simulations and parameter estimation," Procedia IUTAM **16**, 123 (2015).
[27]Aristeia, "Characterization of microbubbles with elastic coating (contrast agents) for medical imaging applications and drug delivery via ultrasound, using theoretical & computational analysis of their static & dynamic response," http://contrast-aristeia.mie.uth.gr, 2015.
[28]A. Lytra, N. Pelekasis, V. Zafiropoulou, T. Zisis, A. Giannakopoulos, V. Sboros, E. Glynos, and V. Koutsos, "Static response of coated microbubbles: Modelling simulations and parameter estimation," in 8th GRACM, Volos, 2015.
[29]E. Buchner Santos, J. K. Morris, E. Glynos, V. Sboros, and V. Koutsos, "Nanomechanical properties of phospholipid microbubbles," Langmuir **28**, 5753 (2012).
[30]R. H. Abou-Saleh, S. A. Peyman, K. Critchley, S. D. Evans, and N. H. Thomson, "Nanomechanics of lipid encapsulated microbubbles with functional coatings," Langmuir **29**, 4096 (2013).
[31]R. Skalak, A. Tozeren, R. P. Zarda, and S. Chien, "Strain energy function of red blood cell membranes," Biophys. J. **13**, 245 (1973).
[32]H. Hertz, "Ueber die Berührung fester elastischer Körper," J. Reine. Angew. Math. (Crelle's Journal) **92**, 156–171 (1882).
[33]K. L. Johnson, K. Kendall, and A. D. Roberts, "Surface energy and the contact of elastic solids," Proc. R. Soc. A **324**, 301 (1971).
[34]U. Seifert and R. Lipowsky, "Adhesion of vesicles," Phys. Rev. A **42**, 4768 (1990).
[35]B. V. Derjaguin, V. M. Muller, and Y. P. Toporov, "Effect of contact deformations on the adhesion of particles," J. Colloid Interface Sci. **53**, 314 (1975).
[36]V. M. Starov and M. G. Velarde, "Surface forces and wetting phenomena," J. Phys.: Condens. Matter **21**, 464121 (2009).
[37]J. N. Israelachvili, *Intermolecular and Surface Forces* (Elsevier Science, 2010).
[38]I. Cantat, K. Kassner, and C. Misbah, "Vesicles in haptotaxis with hydrodynamical dissipation," Eur. Phys. J. E **10**, 175 (2003).
[39]M. J. Blount, M. J. Miksis, and S. H. Davis, "The equilibria of vesicles adhered to substrates by short-ranged potentials," Proc. R. Soc. A **469**, 2012.0729 (2013).
[40]N. T. Chamakos, M. E. Kavousanakis, and A. G. Papathanasiou, "Enabling efficient energy barrier computations of wetting transitions on geometrically patterned surfaces," Soft Matter **9**, 9624 (2013).
[41]S. Komura, K. Tamura, and T. Kato, "Buckling of spherical shells adhering onto a rigid substrate," Eur. Phys. J. E **18**, 343 (2005).
[42]M. P. Neubauer, M. Poehlmann, and A. Fery, "Microcapsule mechanics: From stability to function," Adv. Colloid Interface Sci. **207**, 65 (2014).
[43]D. P. Updike and A. Kalnins, "Axisymmetric behavior of an elastic spherical shell compressed between rigid plates," J. Appl. Mech. **37**, 635 (1970).
[44]D. P. Updike and A. Kalnins, "Contact pressure between an elastic spherical shell and a rigid plate," J. Appl. Mech. **39**, 1110 (1972).
[45]A. Fery and R. Weinkamer, "Mechanical properties of micro- and nanocapsules: Single-capsule measurements," Polymer **48**, 7221 (2007).
[46]R. Mercadé-Prieto, B. Nguyen, R. Allen, D. York, J. A. Preece, T. E. Goodwin, and Z. Zhang, "Determination of the elastic properties of single microcapsules using micromanipulation and finite element modeling," Chem. Eng. Sci. **66**, 2042 (2011).
[47]S. Timoshenko and S. Woinowsky-Krieger, *Theory of Plates and Shells* (McGraw-Hill, 1959).
[48]D. Barthès-Biesel, A. Diaz, and E. Dhenin, "Effect of constitutive laws for two-dimensional membranes on flow-induced capsule deformation," J. Fluid Mech. **460**, 211 (2002).
[49]C. E. Weatherburn, *Differential Geometry of Three Dimensions* (The University Press, 1961).
[50]C. Pozrikidis, *Modeling and Simulation of Capsules and Biological Cells* (Taylor & Francis, 2003).
[51]K. Tsiglifis and N. A. Pelekasis, "Parametric stability and dynamic buckling of an encapsulated microbubble subject to acoustic disturbances," Phys. Fluids **23**, 012102 (2011).
[52]S. Knoche and J. Kierfeld, "Buckling of spherical capsules," Phys. Rev. E **84**, 046608 (2011).
[53]A. Lytra, "Numerical and theoretical study of the static response of coated microbubbles subject to uniform and distributed load: Application on the estimation of the shell elastic properties," Ph.D. thesis, University of Thessaly, 2017, http://thesis.ekt.gr/thesisBookReader/id/40137#page/1/mode/2up.
[54]A. Libai and J. G. Simmonds, *The Nonlinear Theory of Elastic Shells* (Cambridge University Press, 2005).
[55]P. M. Prenter, *Splines and Variational Methods* (Wiley, 1975).
[56]R. Seydel, *From Equilibrium to Chaos: Practical Bifurcation and Stability Analysis* (Elsevier, 1988).
[57]D. P. Updike and A. Kalnins, "Axisymmetric postbuckling and nonsymmetric buckling of a spherical shell compressed between rigid plates," J. Appl. Mech. **39**, 172 (1972).
[58]C. A. Grant, J. E. McKendry, and S. D. Evans, "Temperature dependent stiffness and visco-elastic behaviour of lipid coated microbubbles using atomic force microscopy," Soft Matter **8**, 1321–1326 (2012).
[59]T. Segers, L. de Rond, N. de Jong, M. Borden, and M. Versluis, "Stability of monodisperse phospholipid-coated microbubbles formed by flow-focusing at high production rates," Langmuir **32**, 3937 (2016).
[60]F. Jähnig, "What is the surface tension of a lipid bilayer membrane?," Biophys. J. **71**, 1348 (1996).
[61]F. B. Hildebrand, *Methods of Applied Mathematics* (Dover Publications, 2012).